FIRST PRINCIPLE SIMULATIONS FOR ELECTRONIC STUCTURES AND TRANSPORT PROPERTIES OF EDGE DOPED GRAPHENE NANOSTRUCTURES FOR APPLICATIONS IN GLUCOSE SENSORS

GISHU SEMU TELILA

A THESIS SUBMITTED TO MATERIALS SCIENCE PROGRAM

PRESENTED IN PARTIAL FULFILMENT OF THE RQUIREMENTS FOR

THE DEGREE OF MASTER OF SCIENCE (IN MATERIALS SCIENCE)

ADDIS ABABA UNIVERSITY

ADDIS ABABA, ETHIOPIA

JUNE 2012

Addis Ababa University

School of Graduate Studies

This is to certify that the thesis prepared by Gishu Semu, entitled: first principle simulations for electronic structures and transport properties of edge doped graphene nanostructures for applications in glucose sensors and submitted in partial fulfillment of the requirements for the degree of degree of master of science (in materials science) complies with the regulations of university and meets the accepted standards with respect to originality and quality.

Signed by the Examining Committee:

Examiner Prof. Teketel Yohannes Signature _____ Date 26/06/2012

Examiner Dr. Gebremedhen G/Yesus Signature _____ Date 26/06/2012

Examiner Dr. Tilak Bollepalli Signature _____ Date 26-06-2012

Advisor Prof. Javed Mazher Signature _____ Date 26.06.2012

Abstract

First principle simulation for electronic structures and transport properties of edge doped graphene nanostructures for applications in glucose sensors

Gishu Semu Telila

Addis Ababa University, 2012

Glucose as adsorbed species on edges of the graphene nanostructures are found to create some significant variations among the nanostructure's electronic properties and the changes are fruitfully tapped for futuristic nano-sensing applications. The present study is focused on ab-initio transport measurement for a nano-scale sensor which comprises of either H or O-edge doped zigzag graphene nanoribbons (zGNRs). A range of diverse transport phenomenon is observed by either variation of gating, edge doping, and biomolecular (glucose) attachments or by a combination of all these factors. Our results of these measurements point towards the suitability of ribbon's zigzag edges as glucose attachment sites for the sensing purpose. Furthermore, transformations of conductivity, density of states, and current-voltage characteristics are studied in the nanostructural two-dimensional forms of carbon with foreign atoms doped in or in vicinity of the honeycomb lattice. In addition, we proposed some capable sensing device architectures for exploiting the newly explored unique functionalities. It is important to precisely control and study the density and character of the charge carriers, nature of chemical doping, and biomolecular adsorbates for tailoring the proposed *in-vivo* glucose sensor's properties. First principle two probe methods are used in this work for the nanodevice simulation in conjunction with density functional theory (DFT) and nonequilibrium Green function (NEGF) methods in a standard electron-correlation approximation scheme of local density (LDA).

Acknowledgements

First of all I would like to thank the Almighty God for giving me health, patient, and everything I want by his name. I would like to thank my advisor Prof. Javed Mazher for guiding me through this thesis work, for supporting me with all his expertise on the material, for taking time whenever I came up with questions, for proof reading my work and for always believing in the relevance of our results. Without him, this thesis work would not have been possible. He has been in any moment fully available for discussions and has always provided interesting and stimulating contributions to my research work. So, I believe what I have learnt from him would greatly benefit my future career.

I would like to express my great sincere appreciation and many thank to Prof. Teketel Yohannes, Director for research Addis Ababa University and Chair of Materials Science Program. He primarily introduced and opened me a window to the exciting field of research in graphene during my seminar course work, besides he has given me many graduate courses which are corner stones to my present thesis work. So that became my source of motivation to undertake graphene based research for my thesis work.

Thanks to my classmates, they have directly or indirectly contributed to complete the present thesis work and I am glad to give my thanks to all of them.

Lastly, and most importantly, I would like to thank my sister (Kelemua Urge) and my son, for their love, unconditional understanding, and support me with huge patience.

Table of Contents

List of Tables

List of Figures

CHAPTER ONE

1 INTRODUCTION

Modern techniques of nanosciences and nanostructures allow us to scale down various imperative functional devices like sensors, fast switches, efficient field effect transistors, etc, thus open up new perspectives for their applications [1]. Graphene is a new wonder material for the purpose of nano-sensing that is mainly owing to a rapid change in its electronic properties like charge densities and conductivities, which are mostly governed either by external field effects or by various organic and inorganic foreign functional group attachments to the graphene sheet. Futuristic scientific advancements in the field of graphene based sensor nanoelectronics is expected to grow exponentially due to the device reliability and the ease of mass scale fabrication amongst them. Besides, a true two-dimensional character of the graphene based miniaturized sensing devices have attracted lots of attention of the scientific community. Along with the graphene nanostructures, high mobilities for low energy electrons that is ten times more than that of silicon wafers is also found to be helpful in attaining much more efficient nanoelectronics sensor devices that can operate at low voltages [2].

Moreover, graphene based sensors are efficient enough to sense even the presence of a single molecule. Hence, the graphene has enormous potential for applications in the field of molecular sensing. The present thesis work tries to address the issue of biomolecular sensing and more specifically a useful sensing of a glucose molecule, whose efficient in-vivo sensing is much in demand in areas of diabetics and other medical applications as well as for sugar level testings in various food and nutrition industries. In the thesis work, we have tried to deploy two different types of graphene

nanostructures of zigzag patterned graphene nanoribbons (zGNRs), which are edge doped either by hydrogen (H) or by oxygen (O) for the very purpose of sensor stability. The edge-doped zGNRs are further exposed to varying concentrations of the glucose molecules. The glucose concentrations are marked by number of glucose molecules attached to edges of the zGNRs. We have systematically varied the number of attached glucose molecules from one to six for the ribbons of finite length and studied the electronic structures and the transport properties of the zGNR glucose sensors. We have also performed studies of single and both side edge attachment of glucose with zGNRs, along with a current-voltage behavior of the sensor; first in the absence of the glucose and followed by varying glucose concentrations. Then, the simulational methodology within the DFT-LDA-NEGF framework is used to accomplish all the first principle calculations for the thesis work.

In summary, various types of glucose sensors that are either commercially available or currently at the research and developmental stage are discussed in the Chapter 1 along with description of the structural and the electronic properties of the graphene and the nature and effects of the edge doping either by hydrogen or oxygen on the zGNR material. Besides, a rationale of use of the edge doped zGNRs in these sensors is also discussed along with the relevant doping properties. Chapter 2 contains the objectives of the study. In the Chapter 3 we provide a brief theoretical background on the methods that are relevant for the thesis, and the simulational sample preparations of edge-doped zGNRs with their attachment with the glucose molecules along with a detailed procedure of two probe type sensor. A chapter 4 contains the results and the discussions of the simulational sensor devices. Finally, in the Chapter 5 we present conclusions and future outlooks of the thesis.

1.1 Glucose Sensors

Normal value of blood glucose levels or the blood sugar concentrations vary among different persons because of several factors that can affect a person's blood sugar levels. A homeostatic/insulin mechanism of the person's body, when operating normally, restores the blood sugar level to a narrow range of about 4.4 mmol/L to 6.1 mmol/L. Despite widely variable intervals between meals or the occasional consumption of meals with a substantial carbohydrate load, human blood glucose levels tend to remain within the normal range. However, shortly after eating, the blood glucose level may rise in non-diabetics persons also temporarily up to 7.8 mmol/L or a bit more. However, the levels soon become normal in the body. American Diabetes Association (ADA) recommends a post-meal glucose level of less than 10 mmol/L and fasting plasma glucose of 5 mmol/L to 7.2 mmol/L. Actually, the required amount of glucose in the blood and body fluids is very small and in a healthy adult male of 75 kg with a blood volume of 5 litres, a required blood glucose level is only 5.5 mmol/L that amounts to only 5 grams. Part of the reason of this meager amount is to maintain influx of glucose into cells and enzymes to modify glucose by adding phosphate or other groups [3].

Due to such an importance given to the levels of glucose in both the healthy and the diabetic people, it becomes essential to precisely perform either in-vivo or in-vitro single glucose molecule real time sensing. For in-vivo precise sensing, the graphene exploitation is a good alternative, owing to its organic nature and absence of any side effects of the graphene, which support the in-vivo installation. Final aim of such device implantation is to support the real time drug (insulin) delivery and to gain an

insight of the biological systems apart from novel pharmacological agents that can be tolerated by the living organism.

Recent advances in the insulin pump technology have also created a demand in the area of glucose sensing because of several reasons similar to improvement in the quality of life of insulin pump users. While using a continuous insulin delivery system, users are required to check their blood glucose levels frequently throughout the day. Many current glucose sensors, such as the precision pencil type tester as shown in a Figure 1.1 (left) and the Glucometer Elite XL on the right side of the Figure 1.1, rely on a direct analysis of the blood withdrawn from the tip of a finger. However, many patients complain that these Figure sticks are painful and leave the fingertips swollen and tender for many hours afterwards. Hence the goal of many recent glucose sensing devices is simply to minimize the pain associated with monitoring blood glucose levels. The second reason for the increased demand of novel glucose sensor is that the ability of the insulin pump system to maintain the normal blood glucose levels is only as good as the patient's own manual ability to monitor these levels throughout the day, and adjust his or her insulin pump accordingly. Because of their need to be calibrated often, such devices would only slightly better than that of pathology laboratory tests. However, they would allow insulin pump users to avoid complications while maintaining more physiologic blood glucose levels. Thus traditional insulin pump systems, can potentially lead to insulin mismanagement, often causing mild to severe hypoglycemia. For these reasons, the novel in-vivo glucose sensing field becomes lucrative area for current research activities.

Thus, the recent growth in the area of in-vivo glucose sensing essentially represents the final goal in the treatment of Type I diabetes: an artificial ß-cell. Such a device

would also have the ability to constantly monitor blood glucose levels and respond to low/high levels through the continuous release of insulin into the blood stream. Ideally, all of these functions should be carried out with little or no input from the user to avoid the human errors which is also one of the aims of novel nano sensors. To be incorporated in the animal body, there are some properties that a glucose sensing system must absolutely possess in order to prevent complications. It must be both accurate and precise, with a high reactivity to changes in blood glucose concentrations. It must also have excellent biocompatibility in order to maintain its integrity and efficacy in-vivo for extended periods of time.

Figure1.1: Images of various types and sizes of the commercially available glucose sensors. The precision glucose test strip (left image) and Glucometers (right image) use the blood samples taken from the Figure tips for measurements [3].

1.1.1 Alternate site sensing

The sensors that allow users to test their glucose levels by drawing blood from their arm instead of the tips of their fingers are called as ex-vivo digital glucose sensors as shown in a Figure 1.2 along with its working mechanism. The advantages of such

devices are that they require a smaller volume of the user's blood, that is the required blood volume is 1 μL or less as compared to as much as 4 μL for other devices and they also require less time for each measurement, only 5 seconds compared to as long as 40 seconds for other devices. Because of this, these devices can be used on the arm, where there is a smaller density of nerve endings, and are thus significantly less painful to use. The only limitation to these products is that an arm test may be inaccurate in the 2 hours following a meal or exercise, because the fingertip is more reactive to changes in blood glucose concentration.

Figure 1.2: Images showing the working of ex-vivo digital glucose sensor, the subject's blood can be taken either by puncturing the middle finger (left image) or by venial extraction (central image) followed by subsequent injection into the top sensing quarter of the device (right image) [3].

1.1.2 Transcutaneous sensing

Transcutaneous glucose monitoring systems, such as the Glucowatch are shown in the left of Figure 1.3, and its mechanism is depicted in the right of the Figure 1.3, such type of sensor represents a non-invasive form of continuous glucose sensing, and their

function is based on the principle of reverse ionopheresis, meaning that a low current is applied to a small area of skin in order to extract glucose molecules.

This sensor is an example of both the ex-vivo and the in-vitro sensing devices. So far there are several limitations to such transcutaneous sensing that comprise of a time lag of almost 20 minutes between sensor data and actual blood glucose, poor sensitivity for very low glucose levels, and an eventual irritation at the spot where the electrodes make contact with the skin. These devices often feature an alarm that can be set to sound when glucose levels are above or below a pre-set range, making them an effective way to achieve tighter glucose monitoring in comparison to the alternate sensing. However, in the transcutaneous sensing mechanism, there is an absence of any appropriate way to calibrate the attached insulin delivery device [4].

Figure 1.3: Photograph of a wristwatch type of transcutaneous glucose monitoring systems on the left. The right schematic depicts the schematic of the transcutaneous sensing mechanism. Alternatively it is also known by its common name of Glucowatch [4].

1.1.3 Enzyme based sensing

Another promising method for continuous monitoring of glucose levels are implantable enzymatic sensors, such intravenous glucose sensors can be operated as an open-loop or closed-loop system. As a consequence of, in the open-loop configuration, the sensor data can be accessed and used to adjust insulin delivery by an external programmer through transcutaneous telemetry. Whereas, an algorithm is used to control blood glucose with no input from the patient in the closed loop configuration. However,several reports have shown that the closed-loop configuration is a fairly effective way to maintain normoglycemia [5]. This sensor can also be implanted in the subcutaneous tissue using a specialized tool designed to minimize tissue damage. The sensor is connected by a wire to a pager-sized unit which records data that can later be downloaded onto a computer. The tip of the sensor is made of a membrane, which is selectively permeable to the glucose. Once the glucose passes through the membrane, it is oxidized by an enzyme glucose oxidase. Following this the reduced glucose oxidase can be oxidized by reacting with molecular oxygen, forming hydrogen peroxide as a by-product. At the electrode surface, hydrogen peroxide is farther oxidized into water, generating an electrical current which can be measured and correlated to the glucose concentration. The schematic of this sensing mechanism is presented in a Figure 1.4 which depicts the above mentioned four steps on the specially designed sensor electrode.

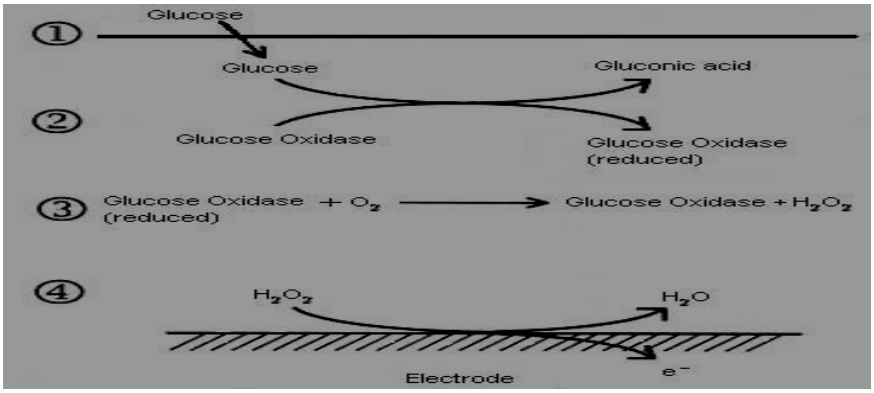

Figure 1.4: A scheme of a typical reaction mechanism deployed over the specially designed electrode among the enzyme based sensors for the purpose of glucose sensing through a change in resistance owing to presence of as formed thin water layer over the surface of the electrode [5].

1.1.4 Strip type Glucose sensors

The strip sensors belongs to a variant of ex-vitro measurement that make use of Benedict's test in which a chemical reagent is used as a test for the presence of reducing sugars in the given sample under laboratory level. Besides, this the pure chemical testing has the ability to recognize the presence of all monosaccharides, disaccharides, lactose and maltose. The copper sulphate of the Benedict's solution reacts with the reducing sugars, and the reagent can be prepared from 100 g of anhydrous sodium carbonate, 173 g of sodium citrate, and 17.3 g of copper (II) sulfate pentahydrate [6].

Mostly this test is used by the pathology labs for the presence of glucose in the urine sample instead of directly on the blood. Therefore, the glucose found in urine is an indication of the diabetes mellitus. Once a reducing sugar is detected in urine, further tests have to be carried out in order to ascertain the proper medication. Most vital

disadvange of the chemical testing is that it never ascertains the presence of glucose for conclusive confirmation of diabetes.

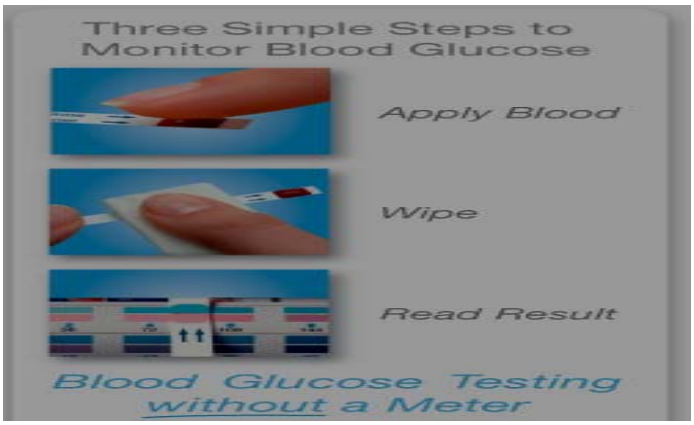

Figure 1.5: A schematic depicting various steps in monitoring the blood glucose leads using the chemical reagent based strip sensors [6].

Table 1.1: Urine tests for the presence of Sugar using chemical reagents.

Benedicts test for sugar presence	**Observation**	**Inference**
Substance in water + 3 ml Benedict's solution, then boil for few minutes and allow cooling.	Red ppt or green ppt or yellow ppt obtained.	Reducing sugar E.g. Glucose is present.
Substance in water + 3 ml Benedict's solution, then boil for few minutes and allow cooling.	Solution remains clear.	Reducing sugar is not present.

1.1.5 Optical sensors (Based on spectroscopic techniques)

A mid-infrared sensor for continuous glucose monitoring in combination with a subcutaneous or a vascular body interface is already a well developed method to meet the demand for reagent-free sensing. Monitoring of human subcutaneous interstitial fluid or whole blood dialysate can also be realized by an ex-vivo arrangement. The

body interface between the subject and the glucose sensing device is usually an implantable micro-dialysis catheter or an extra-corporeal whole blood micro-dialysis device. In this sensor a fluidic system for intermittent sample transport to a flow through micro-cell is used for transporting the biofluid sample to a mini-spectrometer. The body fluids then are dialysed using perfusates at flow rates of 1 µl/min or 5 µl/min, that realized by push-pull operation of a mini-peristaltic pump. As a result of the osmotic exchange of biocompounds between the biofluid and the perfusate, low molecular mass components are harvested. This fibre-optic based sensing system is fully automated and connected with an insulin pump for the desired medication. The major advantage of this approach is its excellent selectivity of the type of sugar and sensitivity to concentration. Nevertheless the sensing system is huge and unportable, and also the in-vivo real time sensing hinders the mobility of the patient in the system. Conversely, as discussed before, the graphene based glucose sensors have the potential to be as sensitive as the fibre-optic fluorometric sensors and at the same time they have the suitability for in-vivo sensing owing to their nano-scale dimensionality and portability. With this motivation for the development of the novel graphene based glucose sensors, we have started this piece of research by using the full potential of the available device simulational aids [7].

1.2 Graphene and its properties

Graphene research is progressing at a remarkable pace, due to the large variety of properties which make graphene extremely exciting, both for fundamental science and for technological applications. Graphite which is the parent compound for graphene has largely been used as lubricants, steel making, and battery components and, of course, as a writing material (pencil). However, it is only around 1950 that the

electronic structure of graphite is studied in depth [8]. The zero-dimensional form of carbon, the fullerene is discovered in 1985 by Harold Kroto, Richard Smalley and Robert Curl [9, 10]. This discovery is an important step into the nanotechnology world. One-dimensional carbon nanotubes (CNT) are discovered by Ijima in 1995 [11]. The two-dimensional form of carbon bounded in a sp^2 configuration that is named as graphene or a single atomic layer of graphite is isolated in 2004 by Giem and co-workers from Manchester University by applying technique of micromechanical cleavage [12]. Graphene has not only smoothened the way for future carbon based electronics, but the charge carrier density can also be tuned continuously from electrons to holes and vice versa. As well as the engineering of high mobility of charge is also possible in graphene. The potential usage of graphene as a nano-sensor is recently explained due to its amazing stability and extraordinary sensitivity to the absorbed species and external fields [13].

1.2.1 Graphene

Graphene is a honeycomb lattice of sp^2-bonded carbon atoms, and the Bravais lattice of its crystal structure has two interlocked triangular sublattices with mirror, time reversal and parity symmetries. The distinct symmetries of the graphene are responsible for linear energy dispersion relationships at six corners of the hexagonal Brillouin zone, which in turn leads to unusual quantum properties in graphene. Especially, a fermionic masslessness, ballisticity, unusually high mobility (largest among the known materials) and unique half-integer quantum Hall effect are frequently reported in graphene [13]. Moreover, as an added consequence of these symmetries, resistive back-scattering in graphene is strongly prohibited leading to long coherence lengths of carriers. Also as an outcome to very high velocities of

charge carriers in graphene the charge carriers at low energy start exhibiting linear energy-momentum dispersion. Thus carriers in graphene can be described as massless Dirac fermions. As a result, the electron scattering processes are suppressed, and thus, the charge carriers can propagate freely on the graphene surface. Furthermore, graphene also combines aspects of semiconductors and metals, and it is a promising replacement for conventional semiconductor materials such as silicon in the nanoelectronics devices. Besides, due to its unique structural, mechanical and electronic properties, graphene has become an important candidate for numerous potential applications, ranging from spintronic devices, gas sensors, nano-composites to transparent electrodes for light emitting diodes, and photovoltaics. Besides, the most of the electronic properties and the chemical reactivity of graphene sheets are originated from characteristic π and π^*orbital. Some of the promising features of graphene include: (i) Very high mobility of electrons in graphene (~15,000 cm^2/Vs.) compared to that in Silicon (~1400 cm^2/Vs.) at room temperature; and such high mobility promises near-ballistic transport and ultrafast switching. (ii) Very low resistivity (~1.0μΩcm), which is about 35% less than the resistivity of Copper; (iii) Very large breaking strength (~40 N/m), and hence stronger than steel and diamond [13,14].

Unlike all other known materials, graphene remains highly stable and its conductivity even enhances when it is cut into ribbons of a nanometer width. Moreover, the advantage of graphene over carbon nanotubes in electronics is its planar two dimensional structures that enable circuit design with standard lithography techniques. Hence, it can be used to make transistors at the true-nanometer scale.

1.2.2 Crystal and Electronic Structure of Graphene

The honeycomb crystal structure of single layer graphene consists of two sublattices that results in a unique band structure for the π-electrons near the Fermi energy, which behave as massless Dirac fermions. Similarly, the valence and conduction bands touch conically at two nonequivalent Dirac points, namely K and K' points, which form a time-reversed pair. The chirality and a Berry phase of π at the two Dirac points provide an environment for highly unconventional and fascinating two-dimensional electronic properties, such as the half-integer quantum Hall effect, the absence of back-scattering phase shift [14]. These two sublattices viz A and B that are triangular lattices and in the xy plane and the unit vectors in real space are $\vec{a_1}$ and $\vec{a_2}$, while the reciprocal lattice vectors are $\vec{b_1}$ and $\vec{b_2}$ as shown in Figure 1.6, given by,

$$a_1 = \frac{a_0}{2}\left(\sqrt{3},1\right) \quad , a_2 = \frac{a_0}{2}\left(\sqrt{3},-1\right) \tag{1.1}$$

$$b_1 = \frac{2\pi}{a_0}\left(\frac{1}{\sqrt{3}},1\right) \quad , \quad b_2 = \frac{2\pi}{a_0}\left(\frac{1}{\sqrt{3}},-1\right) \tag{1.2}$$

where, $a_0 = \sqrt{3}a$ is the lattice constant and interatomic spacing a (C-C = 1.42 Å).

The six corners of the hexagonal BZ form two inequivalent groups of K points. The energy dispersion of π-electrons in graphene is first derived in 1947 by Wallace [15], with in the tight-binding approximation. In this case, the wave function of graphene is a linear combination of Bloch functions for sublattice A it is given by,

$$\phi_A = \left(\frac{1}{\sqrt{N}}\right)\sum R_A \exp\left\{ikR_A\varphi\left(r-r_A\right)\right\} \tag{1.3}$$

and an equivalent function ϕ_B for the B sublattice. Here N is the number of unit cells r_A are the position of the atom A and $\varphi(r-r_A)$ the $2p_z$ orbital of the atom at r_A. The sum runs over all unit cells, i.e. all possible lattice vectors.

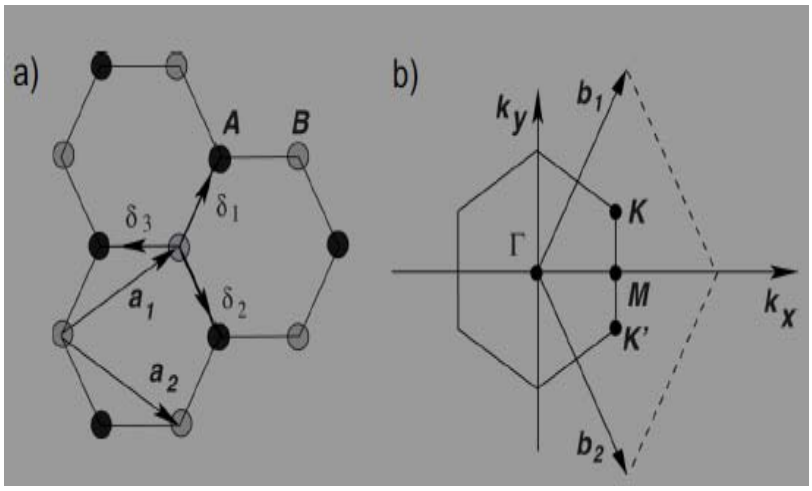

Figure 1.6: (a) Hexagonal lattice structure of graphene in which the Bravais lattice contains carbon atoms (A, B) per unit cell with lattice vectors are $\vec{a_1}$ and $\vec{a_2}$. (b) The reciprocal lattice denoted by the vectors $\vec{b_1}$ and $\vec{b_2}$ .The first Brillouin zone has a hexagonal shape giving rise to high symmetry points (Γ, M, K and K') [14].

In the nearest neighbor approximation (every A site has three nearest B sites, and vice versa), and the energy eigenvalues can be obtained from the equation (1.4) [16, 17].

$$E(k_x,k_y)=\pm\gamma_0\sqrt{1+4\cos\left(\frac{3k_xa}{2}\right)\cos\left(\frac{\sqrt{3}k_ya}{2}\right)+4\cos^2\left(\frac{\sqrt{3}k_ya}{2}\right)} \qquad (1.4)$$

where, γ_0 is the transfer integral between the nearest neighbors (~2.9 eV to 3.1 eV). The two bands are degenerate the two K points given by the reciprocal space vectors, and at these points the dispersion vanishes this is also the Fermi energy level (E_F) of

intrinsic (undoped) graphene. The honeycomb lattice has a unit cell represented in Figure 1.7 by the vectors $\vec{a_1}$ and $\vec{a_2}$. Such that $\left|\vec{a_1}\right|=\left|\vec{a_2}\right|=a$, with $a_0=2.456\,\text{Å}$ [17].

$$K=\frac{2\pi}{a_0}\left(\frac{1}{3},\frac{1}{\sqrt{3}}\right) \quad , K'=\frac{2\pi}{a_0}\left(-\frac{1}{3},\frac{1}{\sqrt{3}}\right) \tag{1.5}$$

The bonding and antibonding of σ bands are well separated in energy (> 10 eV at Γ), and they are not too far away from the Fermi level [18, 19]. Only these two π bands are thus needed to describe the electronic properties of graphene. Atoms of the graphene hexagonal lattice have the overlapping electronic wave functions. However, such an overlap between the p_z orbitals and the s or the p_x and p_y orbitals is strictly zero by symmetry. Consequently, the p_z electrons, which form the π bands in graphene, can be treated independently from the other valence electrons. Within this π-band approximation, it is easy to describe the electronic spectrum of the total Hamiltonian and to obtain the dispersion relations restricted to first-nearest-neighbor interactions as given by the equation (1.4). The Fermi level E_F is chosen as the zero energy level and the Fermi surface is defined by the set of K and K' points. Since the occupied and unoccupied bands touch at the zone corners, the graphene sheet displays a semimetallic, or zero-gap semiconducting character. Moreover the expansion of equation (1.4) at K (K') yields the linear π and π* bands for Dirac fermions given by,

$$E\pm(k)=\pm hv_F|k| \tag{1.6}$$

The π-band electronic dispersion for graphene near the six corners of the 2D hexagonal Brillouin zone is found to be linear. The linear electronic band dispersion leads to the term "massless Dirac fermions" for these carriers, and the Fermi velocity is given by,

$$v_F=\sqrt{3}\gamma_0\, a/2h \tag{1.7}$$

Across the Dirac points, the dispersion relation is found to be linear and the electrons always move at a constant velocity named as the Fermi velocity. i.e., $v_F = 1 \times 10^6 m/s$.

Although there are six symmetry points in the Brillouin zone and only two of them are independent which are the K and the K' points in Figure 1.7. Furthermore, there are two free electrons per unit cell, the π band, which is the valence band, is completely filled and the π* band, which is the conduction band, is completely empty. Consequently, the Fermi energy is exactly at these K and K' points (or at E = 0).

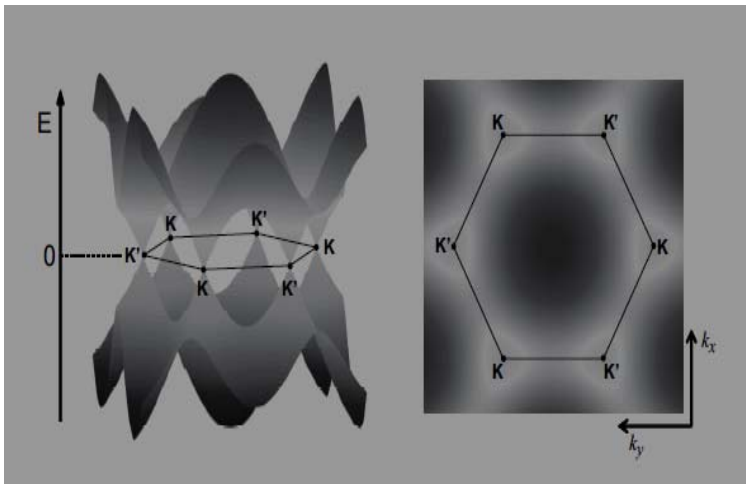

Figure 1.7: The band structure of graphene, which shows the valence band (or the π-band at E < 0) and the conduction band (or the π*-band at E > 0). The states near the K and K' points form independent valleys in momentum space [18].

1.3 Chemical doping and Biomolecular adsorption

Inspite of the fact that, the newly invented nano material Graphene is intrinsically a zero-bandgap material. The process of doping usally induces a bandgap equivalent to that of a semiconducting material. Doping of graphene through molecular charge-transfer processes is triggered by adsorption of either electron-donor or electron-acceptor molecules on the graphene. This process also gives rise to significant

changes in the electronic structure and carrier transport in the graphene. The band structure induced carrier spectrum in graphene monolayers is four-fold degenerate (spin and valley), and the intrinsic sublattice symmetry (two inequivalent Carbon atoms in the unit cell) causes a suppression of resistive back-scattering. These features provide the opportunity to have both spintronic and Dirac electronic functionality on the same device with the theoretical absence of resistive back-scattering. Thus the carrier mobilities in 2D graphene monolayers could be extremely high even at room temperature or even after the adsorption of external atoms. Another advantage of doping is the increase in electrical conductivity which is induced by adsorbed molecule. Recently graphene is used as a highly sensitive solid-state sensor capable of detecting individual molecules [20]. In fact recently boron and nitrogen-doping of graphene has repeatedly appeared in highly sensitive gas sensor reports [21, 22]. It is also experimentally demonstrated that the increase in graphene charge carrier concentration by adsorbed gas molecules can be effectively utilized to make highly sensitive sensors. Because, the sensor property is based on changes in the resistivity due to the molecules adsorbed on graphene nanostructures that act as donors or acceptors. For instance, the sensitivity of NH_3, CO, and H_2O up to 1 ppb (parts per 10^9) is demonstrated, and even the much higher sensitivity of an individual N_2O molecule is suggested [23].

The demonstration of these excellent sensing properties of graphene is due to the following reasons: (i) Graphene is a single atomic layer of graphite with negligible volume and comprises only of surfaces. Thus this leads to maximum possible interaction between the surface dopants and adsorbates even grater than CNTs; (ii) Graphene is a semimetellic with much smaller band gap energy E_g compared to CNT. Hence, it has extremely low noise [23, 24]. As results, a little change of carrier

concentration can cause a notable variation of electrical conductivity; (iii) Graphene has limited crystalline defects which ensure a low level of thermal defect noise [23, 24].

Hence, graphene has promising physisorption properties which are also proved in earlier reports for the hydrogen doping [24]. In which, even a single molecule adsorbed on its surface is found to cause a local change in the carrier density and the resistance. Thus imparting a high sensitivity for such graphene sensors Graphene researchers have also demonstrated a good sensitivity for biomolecules and aromatic ring structures, NH_3, NO_2, and dinitrotoluene adsorbates [25]. It is theoretically found that the aluminum-doped graphene strongly chemisorbs CO molecules due to formation of Al-CO bonds, thus Al-doped graphene is a potential candidate for the detection of CO [26]. The sensors which are prepared by using suspended graphene (in an aqueous solution) provide reduced noise levels due to the absence of interactions with the substrate [26]. The sensitivity and selectivity of such sensors can be highly increased by using graphene doped with particular species like phosphorus, boron, oxygen, hydrogen, and nitrogen [27]. Like wise the stability of graphene nano structures (nanoribbons) can also be increased by H and O doping as edge passivation. With this motivation, we have modeled a range of biomolecular (Glucose) doped graphene samples in the thesis work by employing the first principle simulation of electronic structures and transport properties of the edge doped zGNRs. We carried out density functional theory (DFT) calculations to understand the effect of substitutional H and O edge doping on the physical properties of graphene ribbons.

1.4 Graphene Nanoribbons (GNRs)

Finite termination of graphene with smooth edges produces quasi one-dimensional nano-structures called as graphene nanoribbons (GNRs). A numerous theoretical studies on pure and modified GNRs show exciting magnetic, optical and spin filter properties with advanced device applications. Different geometrical terminations of two-dimensional graphene lattice lead to two distinct edge geometries, namely, zigzag and armchair with largely varying properties originating from different boundary conditions as shown in Figure 1.8. Depending upon the pattern of un-bonded edges, the ribbons can have either a zigzag or armchair configuration. Theoretical calculations predict that zGNRs are always metallic while aGNRs can be either metallic or semiconducting, depending on their width [28]. However, recent density functional theory calculations show that aGNRs are semiconducting and exhibit an energy gap scaling with the inverse of the GNRs width [29].

The π-network of graphene nanoribbons still consists of sp^2 bonded carbons, but the carbon atoms at the edges have only two neighbors, thereby developing many sp carbon bonds and unsaturated dangling bonds. So disruption of the sp^2 carbon network at the edges generates localized states. The structure, lattice orientation and proportion of the sp^2 and sp hybridization of the armchair and zigzag edges are different; consequently, their electronic properties differ, particularly in the formation of localized states. The as noted distinction of the electronic properties between the zigzag and armchair edges is predicted to create localized edge states near the Fermi level, so that zigzag edge exhibits localized states, whereas the armchair edges do not induce such localized states. All in all, such disparity is one of the reasons of our choice of zigzag edge device in preference to armchair edge [30, 32].

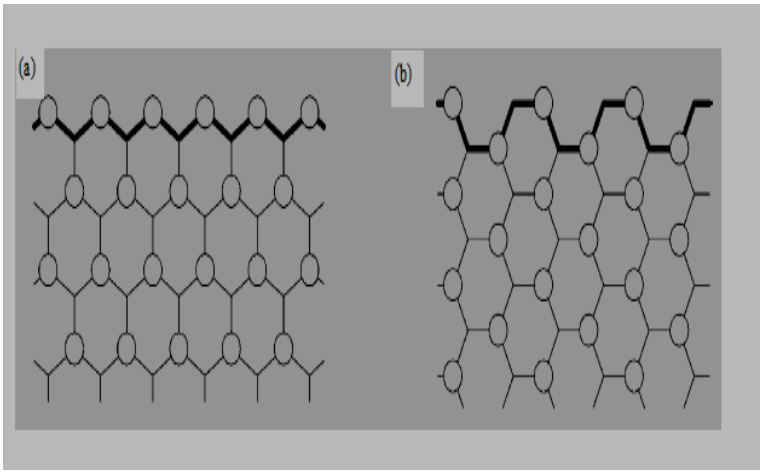

Figure 1.8: Two types of graphene nanoribbons edges (a) Zigzag edge (zGNR), (b) Armchair edge (aGNR) [28].

1.4.1 Edge doping of zigzag GNRs by H and O atoms

Due to finite termination, the bipartite nature of the extended two dimensional graphene lattices gets destroyed and the dangling bonds at the GNR's edge atoms, originate from the unsatisfied valency. These dangling bonds impart some unique characteristics to the edge atoms which are very different from the bulk carbons. The edge atoms now become more reactive in comparison to the bulk; hence the GNRs are modeled and stabilized with negative onsite energy by making use of hydrogen edge passivation at the GNRs edges [33]. Thus the edge passivation can also be modeled by considering the modified onsite energies at the edges [34]. Actually, the passivation of edge carbons by foreign atoms like hydrogen is already very well captured within the first-principles calculations [35]. In the presence of such passivation, the bonding characteristics change at the edges, leading to the modification of onsite energies at the edge carbon atoms, in comparison to the bulk [36]. Several studies indicate that the Hydrogen (H) termination at the edges brings

one of the most stable configurations of the zGNRs owing to its simplistic planar structure [37].

Inspite of the edge passivation by H, the realistic edge chemistry quite often is not covered comprehensively. More edge chemistry effects should be considered for more realistic modeling of GNRs. Edge passivation by H_2, such that all the C atoms of each edge of zGNR are bonded with two H atoms, open up a clear energy gap and induces small amount of magnetism for small widths nanoribbons [38]. Lee et al. [39], calculated the electronic band structures of H and H_2 edge-hydrogenated zigzag graphene nanoribbons (zGNRs) as well as C-O-C edge oxidized zGNRs, and found that the ether (C-O-C) group results in band structures similar to those of sp^3 hybridization of H_2 edge. However, most of the previous studies are mainly focused on the changes in electronic band structures due the edge chemistry of zGNRs, the transport properties have yet not been investigated in details.

1.4.2 Effects of edge doping on electronic properties of zGNRs

Oxidation is found to be the most abundant reaction occurred at the zGNR edges [40]. Recently, the stability and energy gap of edge oxidized zGNRs have been calculated using the ab initio method [40]. In that study, the calculated band gaps are in the range of 0.77 eV to 1.05 eV for most edge terminations. Specifically, the band gap of the 8-zGNR with ideal C-H termination is 1 eV, which is significantly larger than the LDA band gap of 0.3 eV. Another research group, which has studied the zGNR band gap with edge functionalizations by NH_2, OH, COOH, and NO_2 found the zGNR gap variations of the order of 0.26 eV [41]. We have concluded that most of them show a semiconductor like band gap, but O functionalization shows the metallic density of states with small gaps. Since materials are usually transformed into insulators upon

oxidation, and these theoretical reports have shown the seemingly unexpected result that certain oxidized GNRs have a semimetallic gap [42], hence in the thesis we have tried to address the issue of O-edge doping. The recent theoretical study, on edge functionalized graphene finite cluster has shown that the p orbital of an oxygen atom participate in the π-electron system to cause gap states [43]. However, the DOS alone is not enough to determine the metallic or semiconducting character of the system, because localized states may appear near the Fermi level resulting in a zero gap [44]. Therefore, it is important to calculate band dispersion relations for edge-oxidized GNRs for understanding the transport property. Even though the large band gaps of edge-oxidized GNRs are reported [45], the density of states and the origins of the electronic structures near the Fermi level have not been investigated in detail.

Earlier, the stability of different edge geometries of zGNR in the presence of H, O, N, and CO, has already been investigated and reported [46]. In these reports the edge carbon atoms are mostly considered as doping sites, since these are by far the most reactive sites in GNRs. The dopants adsorption energy for the edge configurations can be calculated as; $E_{ads}=E_{ribb+H}-N_H E_H-E_{ribb}$ (1.8)

where, E_{ribb+H} is the total energy of the ribbon with the adsorbed H atom, N_H is the number of doped hydrogen and E_H is the total energy of the doped atom in the vacuum. To avoid the invalid DFT description of the dopants, their total energies in the vacuum phase are mostly used [47]. From the calculations it has been found that the atomic oxygen has the highest binding energy in all edge configurations. Besides the standard zigzag for which the high reactivity is well established, the armchair ribbon at specific widths is also found to be very reactive. It has been attributed that for the zigzag case the peak in the density of states is present close to the Fermi

energy. Also it has been found that the oxygen and hydrogen passivation of the edges usally acquire a lower energy configuration and thus bring stability to zGNRs [48].

The adsorption energies also provide information on the strength of the interaction once a given edge configuration has been formed. The thermodynamic stability of an edge in the presence of dopants and the energetic cost of forming the edge itself have to be taken into account [48]. Since zigzag edges saturated with oxygen atoms are found to be the most stable in the ground state and vibrational properties are also investigated and compared to the well studied hydrogen-passivated edge [49].

To further illustrate the effects of edge doping we have reproduced the Kohn-Sham band structure for the oxygen edge saturated GNR in a Figure.1.9 [49]. The ground state is found to be spin paired and metallic in contrast to that in the hydrogen passivation. The two states at the Fermi level are localized at the edges and have weight also on the p orbital of the oxygen atoms. In particular, one state decays into the GNRs with weight only on one sublattice (left inset of Figure 1.9), while the other is almost completely localized on the out of plane p oxygen orbital (right inset of Figure. 1.9).This is different from the hydrogen-saturated case, in which the edge states are localized on the edge carbon atoms only [49]. Hence, the presence of such contrast in doping related properties prompt us to investigate the zGNRs electronic properties with edge-chemistry modifications by H and O atoms, using the ab initio DFT method within LDA.

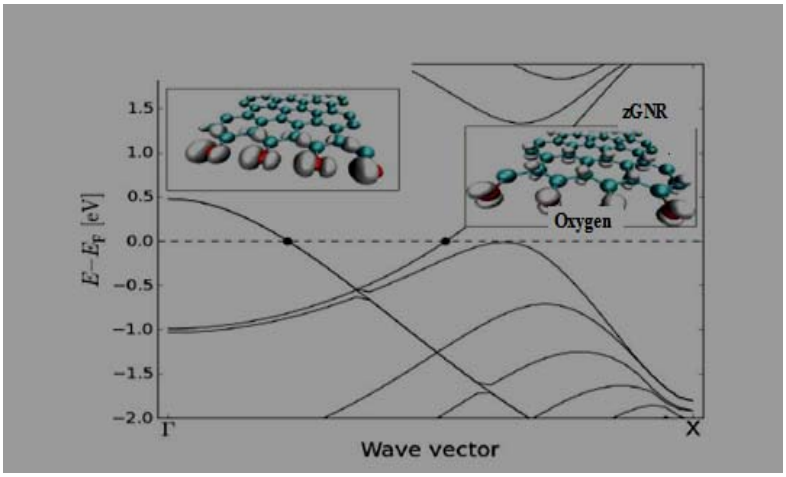

Figure 1.9: Band structure of a 22Å wide zigzag GNR doped with oxygen. The two projected density of states of wave vector values insets show the states corresponding to the bands crossing the Fermi level, marked by black circles [49].

1.5 Density of States (DOS) in Nanostructures

The density of states of a system describes the number of states at each energy level that are available to be occupied. So, a high DOS at a specific energy level means that there are many states available for occupation. For instance a DOS of zero means that no states can be occupied at that energy level. There fore, the states in the bands and their dependence on energy are described by the density of states. However, as result of quantum confinement in different directions, there is a change in wave function describing the behavior of electrons and holes and consequently the number of state per unit energy, i.e. the density of state changes as a function of energy (E) of the particle. Generally, the density of state depends on the dimension of the nano-structure and the corresponding wave vector dispersion. For instance in the case of a bulk-material, the density of state increases with energy of the parabolic law. There

fore, for a three dimensional bulk-material, the DOS is defined as the number of available electronic state per volume per unit energy (E). It is given by;

$$\rho_{DOS}^{3D}(E)=\frac{1}{2\pi^2}\left(\frac{2m^*}{h^2}\right)^{3/2}\sqrt{E} \tag{1.9}$$

Where as in case of two dimensional nano-structure (or quantum well) the carrier movement is restricted to a plan (the third direction determines the quantum confinement direction). So, a quantum well is a nanostructure where there are two directions for the movement of particles, while the third direction determines the quantum confinement direction, and given by:

$$\rho_{DOS}^{2D}(E)=\frac{m^*}{\pi h^2}E \tag{1.10}$$

Further reduction in the dimension of a system ends up in quantum-wire. Examples of such one dimensional structure include nano-tube, semiconductor nano-wire, and nano-rods. For quantum-wire (particles are free to move in only one direction and the two sides are confined) the DOS is defined as the availability of electronic state per unit length per unit energy [50], and given by;

$$\rho_{DOS}^{1D}(E)=\frac{1}{\pi h}\sqrt{\frac{m^*}{2E}} \tag{1.11}$$

Finally, for the zero dimensional system (or quantum dot), the confinement is along all three dimensions and the DOS becomes a delta function. In the zero-dimension the electron are confined in their motion in all three direction or named as quantum dot, and so, a quantum dot has all the three dimensions in the nano range. This means, there is a total confinement in each direction and particles cannot move freely anywhere [50, 51].

$$\rho_{DOS}^{0D}(E)=2\delta(E-E_0) \tag{1.12}$$

1.6 Equilibrium Conductance in Nano-devices

The Fano resonance coupling (FR) is a universal physical phenomenon, which has historically been discovered in atomic physics as asymmetric line profiles in the spectra of rare gases [52].The Fano resonance is a consequence of interference accompanied by a localized state and continuum state that results in an antisymmetric line shape of the resonance created by the localized state [53]. Now a day, the Fano resonances have also been observed in condensed matter physics, nano-materials sciences and nano-electronics, both theoretically and experimentally [54]. So, this phenomenon can also naturally arises in a coherent electrical transport through a nanostructured two probe device, in which a central region of the device is comprises of the nanomaterial or a molecule having discrete energy states coupled with continuum states of electrodes. Such a situation creates the Fano resonances near the Fermi level that often strongly improve an electron through the nano-device [55]. A basic condition for the Fano resonance is a presence of at least two scattering channels in the form of a discrete level and a broad continuum band in proximity to each other, which is often the case of nano-devices' left and right electrodes and the central scattering region of the nano device [55].

The nature of two conduction channels in these mesoscopic systems is highly sensitive to geometries of nano devices under consideration. Similarly, when nanostructures are sandiwiched in two electrodes, a different kind of strong charge coupling happened due to formation of strong bonds in between atomic contacts of the central scattering region (CR), the left (L), and the right (R) electrodes [56,57]. As aresult of the strong coupling some discrete physical traits usually found in the isolated nanostructure like singular energy levels become broadened in the strongly

coupled nanostructure. Rarely, depending upon the amount of charge transfer from electrodes, if these broad energy levels are aligned with chemical potentials of attached electrodes, we usually get small conduction states at the Fermi level of the nanostructure. Thus, the band realignment of the nanostructure is responsible for low energy charge carrier conduction in the two probe devices [58]. One of the ways to explore their signatures is to study density of states and non-equilibrium electron-transmission spectra of the nano device having a quantum confined central region. Moreover various atomistic ab-initio modeling studies show that bulk contacts are absent in the nano device instead only pure atomic scale contacts are formed [54].This implies that the I–V characteristics and the rectification behavior in the device mainly depends upon (i) Electrode materials and their dimensionality, (ii) Singularities present in the density of electronic states of the nanostructure located at the central region of the device, (iii) Interfaces and a contact geometry of the electrodes and the central region, and (iv) A coupling strength between the two ends of the central region with electrodes [58]. Often the strong coupling results in sharp and intense DOS peaks near the Fermi level and the weak coupling gives a broader DOS resonant states. This effect is reported in the density of states and the transmission energy spectra along with I–V measurements [54, 55], where an ohmic contact is observed instead of a rectification at the nanometallic/nano-semiconductor atomic interface. In fact, Fano line shapes are also observed in a differential electrical conductance (dV/dI) plot with bias voltage during a tunneling course using a scanning tunneling microscope and through an impurity atom on a metallic surface [56]. Quite the opposite, the Fano anti resonance are reported in the density of states and the transmission spectrum of nano-devices at the Fermi level when an injection of states from electrodes to the central

region is destructive in its interference with states present in the central region, which is usally manifested in the rectifying behavior of the nano devices [58].

CHAPTER TWO

2 Objectives

2.1 General Objectives

The general objective of this work is to model the electronic structures and transport properties of edge doped graphene nanostructures using first principle simulation for applications in glucose sensors.

2.2 Specific Objectives

1. To model the samples of zGNRs edge doped by hydrogen and oxygen.

2. To model the 2 probe nano sensors of doped graphene nanoribbons in the central region of the sensor and to optimize the device configurations.

3. To study the adsorption of glucose on the GNRs at various concentrations by;

   (i) Attaching the glucose on only one side edge of zGNRs.

   (ii) Attaching the glucose on both side edges of zGNRs.

4. To study the changes in the electronic density of states of the GNRs sensor on doping and glucose attachment.

5. To study the changes in the I–V characters of the GNRs sensor for various concentrations of glucose attachment on the central region of the device.

6. To propose a scheme for graphene based unique sensor architecture by exploiting the newly explored novel functionalities and to study glucose sensor performance based on precise control of the density and character of its charge carriers.

CHAPTER THREE

3 Simulational Methodologies

The physical, chemical and electronic properties of a system can be easily studied by using well defined electronic energy band structure. As a result the study of electronic energy states of the system has been a main issue of research amongst the scientists. Now a day theoretical methods like First Principle (Ab initio) Density functional Theory (DFT) techniques are developed for the systematic study of the electronic structure, with the help of specially developed software tools. Therefore, based on these modern theoretical methods, it has been possible not only to investigate the electronic properties, but also to understand the charge carrier transport behaviour in a much better manner. Moreover, the simulation and modeling features of these software tools are quite useful, particularly in the studies of nanomaterials and nanoelectronics. In this section we briefly make an effort to describe the simulational methodologies used for such study, along with the techniques of sample preparations and the softwares used.

3.1 Ab-initio Theoretical Methods

The biggest difficulty in the modern electronic structures theory is to find an appropriate approach to describe electron correlation interaction. In this chapter, we describe a brief overview of the electronic structure theory, ab-initio density functional theory and non-equilibrium Green's function method.

Ab initio many-body quantum mechanical calculations are crucially important to our understanding of the behavior of atomic, molecular, and condensed matter systems, and this method is a computational method based on quantum mechanical principles

[59]. There are several approximations related with ab-initio calculations, because of almost always the basis set used to solve the Schrödinger equation is not complete, and it is approximated that it does not span the Hilbert space associated with ionization and scattering processes completely. But, in the Hartree–Fock and the Configuration Interaction (CI) methods, the approximation allows one to treat the Schrödinger equation as an eigenvalue equation of the electronic molecular Hamiltonian, with a discrete set of solutions, in which the instantaneous Coulombic electron-electron repulsion is not specifically taken into account. Thus, only its average effect (mean field) is included in the calculation. Therefore, the obtained approximate energies, expressed in terms of the system's wave function, are always equal to or greater than the exact energy, and tend to a limiting value called the Hartree–Fock limit as the size of the basis is increased. Thus, Hartree-Fock does not provide exact solutions to the Schrödinger equation, no matter how large a basis set we use. Many types of calculations begin with a Hartree–Fock calculation and subsequently corrected for electron-electron repulsion, and usally referred as correlation approximations. The procedure of simulating physical properties of system by using quantum mechanics is just the procedure of solving many-body Schrödinger equation of the system. The Hamiltonian of a typical many particle system can be written as follows,

$$H=H_e+H_I+H_{eI} \tag{3.1}$$

Where:

$$H_e=\sum_i \frac{p_i^2}{2m_e}+\sum_{i<j} V_{ee}\left(r_i-r_j\right) \tag{3.2}$$

$$H_I=\sum_I \frac{p_I^2}{2M}+\sum_{I<J} V_{II}\left(r_I-r_J\right) \tag{3.3}$$

$$H_{eI}=\sum_{iI} V_{eI}\left(R_I-R_i\right) \tag{3.4}$$

here, r_i and R_I are the coordinates of the i^{th} electron and the I^{th} nucleus, V_{ee} , V_{II} and V_{eI} represent the interactions between electrons, nuclei and electron-nucleus, respectively. Further consideration about other boundary conditions, such as relativistic effects, spin, or electromagnetic filed, could be added as terms of Hamiltonian. Owing to the complexity of the problem, it is obvious that considering all the degrees of freedom equally from an "ab-initio" manner is impossible. Thus various approximations are necessary to reduce the calculation into an acceptable level.

3.2 Density Functional Theory

Density Functional Theory is an approach to the quantum mechanical many-body problem, where the system of interacting electrons is mapped onto an effective non-interacting system with the same total density. Basically, Hohenberg-Kohn and Kohn-Sham showed that the ground-state energy of an N-electron system is a functional of the electron density n(r). Besides, in DFT the electrons are represented by one-body wave functions, which satisfy Schrödinger-like equations;

$$\left[-N^2+V_N\left(r\right)+V_C\left[n\left(r\right)\right]+V_{XC}\left[n\left(r\right)\right]\right]\psi_i\left(r\right)=\varepsilon_i\psi_i\left(r\right) \tag{3.5}$$

Where i = 1, . . ., N, The first term represents the kinetic energy of a system of non-interacting electrons; the second is the potential due to all nuclei; the third is the classical Coulomb energy, often referred as the Hartree term; and the fourth, the so-called exchange and correlation potential accounts for the Pauli Exclusion Principle.

The term V_{XC}, includes the difference between the kinetic energy of a system of independent electrons and the kinetic energy of the actual interacting system with the

same density [60]. In the modeling of atomic or molecular systems, the most common strategy relies on the approximate solutions of these Schrödinger equations. Thus the DFT has been established as one of the most widely used first-principles methods in nanomaterial science.

The original idea of density functional theory is proposed by Thomas and Fermi, where the kinetic energy term is expressed with an explicit functional of electron density n(r) alone [61]. However, Dirac took into account the local approximation of electron exchange and a correlation interaction, which is absent in Thomas-Fermi approximation, the new scheme is called Thomas-Fermi-Dirac approximation and the energy functional is expressed as the total energy of the electrons is the sum of their kinetic and potential energies,

$$E=T+U_{eN}+U_{ee},$$

$$E=C_F\int\left[n(r)\right]^{5/3}d^3r+\int n(r)V_N(r)\,d^3r+\frac{1}{2}e^2\int\frac{n(r)n(r')}{|r-r'|}d^3r\,d^3r' \qquad (3.6)$$

where the first term is the total kinetic energy of the electrons, the second term is the potential energy of an atom's electrons due to the electrical attraction of the positively charged nucleus, the third term is the potential energy of the electrons due to their mutual electric repulsion and $C_F=\frac{3h^2}{10m_e}\left(\frac{3}{8\pi}\right)^{2/3}$.

Hohenberg and Kohn (HK) further proposed that all properties of a system can be deduced from the ground state electronic density only and that this density can be found by minimizing the expectation value of the Hamiltonian as a functional of the electronic density. It is commonly accepted that the two theorems proposed by Hohenberg and Kohn are the onset of modern density functional theory [62]. So, the Hohenberg-Kohn theorems are applicable on any system consisting of electrons

moving under the influence of an external potential $V_{ext}(r)$ and can be stated simply as follows:

Theorem I: "For any systems of N-interacting electrons, any of its physical properties are completely determined by the ground state electron density n(r)." i.e., $E_{GS}=E\left[n\left(r\right)\right]$

Theorem II: "The global minimum of energy functional is the ground state energy, and the corresponding electron density is the ground state density." i.e., $E_{GS}=E[n(r)]=\min\left\{E[n(r)]\right\}$.

We can write the Hamiltonian of any many-electron system as,

$$H=-\frac{1}{2}\sum_{i}\tilde{N}^{2}+\sum_{i}V_{ext}(r)+\frac{1}{2}\sum_{i\neq j}\frac{1}{\left|r_i-r_j\right|} \tag{3.7}$$

Now the energy functional can be expressed as,

$$E_{HK}\left[n\right]=T\left[n\right]+E_{int}\left[n\right]+\int V_{ext}\left(r\right)n\left(r\right)dr+E_{II} \tag{3.8}$$

$$E_{HK}\left[n\right]=F_{HK}\left[n\right]+\int V_{ext}\left(r\right)n\left(r\right)dr+E_{II} \tag{3.9}$$

Where E_{II} is nucleus-nucleus interaction, $F_{HK}[n]$ is system internal energy, including electron kinetic energy, potential energy and interaction energy.

In order to solve the above problem computationally, Kohn-Sham (KS) proposed a numerical approach for self consistent calculation of density. They associated a system of N-interacting electrons evolving in an external potential V_{ext} (r) with aground-state density n(r), to an auxiliary system of N non-interacting electrons evolving in an effective external potential $V_{eff}[n]$, and having the same ground-state density n(r). In other words, in order to evaluate the kinetic energy of N non-interacting particles given only their density distribution n(r), they simply found the

corresponding potential, called $V_{eff}[n]$, On this basis, Kohn-Sham showed that n(r) can be obtained by solving a set of one-particle Schrödinger equations (the Kohn-Sham equation) is given by,

$$\left(\frac{-h^2}{2m}N^2+V_{eff}(r)\right)\psi_i(r)=\varepsilon_i\psi_i(r) \tag{3.10}$$

The first term describes the kinetic energy of the electron. The second term describes an effective potential energy of the electron moving in the mean field from the other electrons, where the other electrons are described in terms of the total electron density.

In KS scheme all the interactions between electrons are classified into an exchange-correlation (XC) term. The ground state density and other properties can be obtained by solving the non-interacting system in the density dependent one-particle effective potential $V_{eff}[n]$. Thus the exact ground-state density is obtained in terms of the N lowest-energy solutions of equation (3.10) and given by,

$$n(r)=\sum_i^N\left|\psi_i(r)\right|^2 \tag{3.11}$$

The central statement behind the Kohn and Sham approach is that an exact mapping of the interacting problem onto a non-interacting problem is always possible. The states ψ_i, here are ordered so that the energies ε_i, are non–decreasing [63].The effective potential has three contributions:

$$V_{eff}[n]=V_H[n]+V_{XC}[n]+V_{ext} \tag{3.12}$$

The first term, $V_H[n]$ is the Hartree potential due to the mean-field electrostatic interaction, and the second term, $V_{XC}[n]$ is the exchange-correlation potential caused by the quantum mechanical nature of the electrons, $V_{ext}(r)$ represents any other electro-static interactions in the system [63].

3.3 Local Density Approximation

Local-Density Approximation (LDA) approximates the exchange-correlation (XC) energy functional and it also depend only upon the value of the electronic density n(r) at each point in space. In LDA the functional is based on the homogeneous electron gas HEG approximation, which is then applied to more realistic systems. In general, for a spin-unpolarized system, a local-density approximation for the exchange-correlation energy is written as,

$$E_{XC}^{LDA}[\rho]=\int \rho(r)\varepsilon_{XC}(\rho)dr \tag{3.13}$$

Where ρ is the electronic density and ε_{XC}, the exchange-correlation energy density, is a function of the density alone. The exchange-correlation energy is decomposed into exchange and correlation terms linearly,

$$E_{XC}=E_X+E_C \tag{3.14}$$

So that separate expressions for E_x and E_c are required. The exchange term takes on a simple analytic form for the HEG. Only limiting expressions for the correlation density are known exactly, leading to numerous different approximations for correlation energy E_C. Local-density approximations are important in the construction of more sophisticated approximations to the exchange-correlation energy [64].

3.4 Non-Equilibrium Green's Function and I–V Calculations

First-principles calculation brought a reliable approach which is popularized and applied in many areas of research in the recent decades. However, traditional first-principles methods also possesses its limitations, for example, only finite sized systems or infinite systems with internal periodicity can be calculated, in addition,

these systems must be in equilibrium. In this context, systems in nano electronics, which are non-equilibrium, non-periodic, and infinite with open boundary conditions could not be treated properly by using these traditional methods. However, such systems can be treated properly by using Non-Equilibrium Green's function (NEGF) technique and calculations of the electron transport properties can be performed numerically by combining it with DFT [65].

A typical open system in nano electronics can be simplified into a model shown in Figure 3.1, where C, L and R represent, the central region, the left and right electrodes. Both the electrodes are semi-infinite and extend periodically to the left and right, respectively. It is commonly assumed that there is no direct interaction between the left and right electrodes, which can be assured by including sufficient large number of layers from each electrode into the central region.

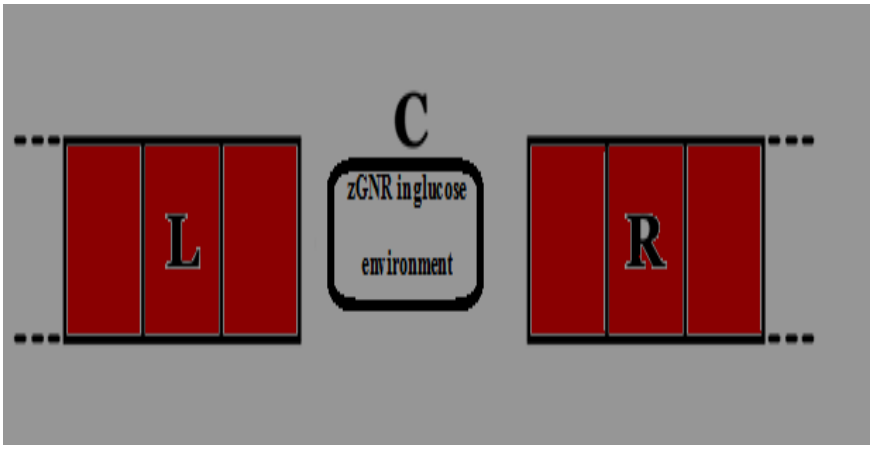

Figure 3.1: Two probe L-C-R device .The central region C coupled with the left (L) and the right (R) leads. Both left and right leads are periodic only in the direction moving away from the central region [65].

Following this in this approach we apply formulation for exactly evaluation of the current using Landauer's type formula; the current under steady state approximation is given by [66];

$$I(V_b) = -\frac{2e^2}{h}\int_{-\infty}^{+\infty} T(E,V_b)\left[f(E-\mu_L) - f(E-\mu_R)\right]dE,\mu \tag{3.15}$$

Where $\mu_{L/R}$ is the chemical potential of left /right electrode of Figure 3.1, f is Fermi-Dirac distribution function; T (E, V_b) is the transmission probability of injecting electrons with energy E when a bias voltage V_b is imposed. Transmission function can be calculated directly from the Green's function of the scattering region.

3.5 Simulation Methodology

Nowadays, Nano-Simulation and Modeling has become an inseparable part of nanotechnological research as the scientific community has realized the maximum importance of theory and modeling along with the experimental work. Today, much advanced, user friendly and specifically designed computational and simulation softwares have provided the essential tool in order to perform in depth study and analysis of nanostructured materials. Moreover, they provide the much needed insight, in order to understand, predict and to precisely exploit their novel properties for the desired experimental and commercial applications. Nanosimulation and Modeling can significantly reduce the time, money and manpower required to carry out actual experimental work and the characterization to validate the results, by providing valuable guidance regarding the best suitable and practically viable combination, configuration and stable nanostructure through its computational and simulational results.

3.5.1 Methodology for Atomistic Simulations

3.5.1.1 SIESTA

SIESTA (Spanish Initiative for Electronic Simulations with Thousands of Atoms) is both a method and Computer program implementations, to perform electronic structures calculations and ab-initio molecular dynamics simulation of molecules and solids. It is a numerical implementation of DFT constructed on a non-orthogonal localized atomic orbital basis set. SIESTA also solves problems at the level of DFT; these problems are, generally, related to ground-state properties. Energy/volume curves, phase diagrams, phonons, molecular dynamics are all related to ground-state properties [67]. Main characteristics of SIESTA are: (a) It uses the standard Kohn-Sham self-consistent density functional method in the LDA or generalized gradient approximation (GGA), (b) It uses norm-conserving pseudopotentials in their fully non local form, (c) It uses atomic orbitals as a basis set, allowing unlimited multiple-zeta and angular momenta, polarization and off-site orbitals, (d) Projects the electron wave functions and density onto a real-space grid in order to calculate the Hartree and exchange-correlation potentials and their matrix elements and (e) Simulations with several hundred atoms are feasible with modest workstations.

TranSIESTA is a combination of NEGF with the DFT code SIESTA. The electrostatic potential is calculated by solving the Poisson equation in k-space superimposing to the Hartree potential a linear potential ramp, while the surface Green's functions are calculated by direct integration. TranSIESTA allows the calculation of current-induced forces and therefore study the mechanical stability of current carrying nano-devices.

3.5.1.2 Virtual Nano Lab (VNL) and Atomistix ToolKit (ATK) software

Quantum Wise provides two different interfaces for performing electronic transport calculations: Atomistic Toolkit (ATK), which is a first principle electronic structures program based on TranSIESTA code, and Virtual NanoLab (VNL), which is a graphical user interface (GUI), is the most appealing option, because of its intuitive ease of use [68].

Atomistix ToolKit is a library of atomic scale modeling techniques that can be used to calculate a wide range of properties of nanoscale systems. The most unique features are the ability to calculate the electrical properties of nanoscale devices. The description of the electronic structure in ATK is based on DFT and an important ingredient in the calculations is the approximation used for the exchange–correlation functional [69]. ATK gives us access to a powerful set of modeling tools for investigating a variety of nanoscale systems such as molecules, bulk and two-probe systems. The systems may contain nanowires, nanotubes, graphene, semiconductors, metals, and the calculations are based on the DFT, Classical potentials, and NEGF [69]. Moreover, ATK can be used to calculate many different properties of the system, including electronic current, voltage drop, transmission coefficients, electron density, etc. A modeling study generally consists of three parts: primary, setting up the calculation, next, running the calculation, and, finally, analyzing the output of the calculation [69, 70].

Virtual nano lab gives us access to a powerful set of modeling tools for investigating nanoscale structures through a user friendly graphical interface. The VNL software uses advanced software design and numerical methods to find solutions of the fundamental quantum mechanical equations describing the electronic properties of nanoscale objects by use of the techniques DFT and NEGF. Based on the these

techniques, VNL can simulate the detailed electronic structures and transport properties of molecules, bulk, crystals, nanotubes, and two-probe devices. The work flow with VNL is: (i) First we set up our system of the study using either of the Bulk Builder, the Crystal Cupboard, or the Atomic Manipulator tools. (ii) After setting up our system, we specify the details of the DFT method that should be applied to our system. (iii) Once the DFT method has been defined, we select the physical properties that should be extracted from the calculation in the NanoLanguage Scripter tool. (iv)The calculation is then performed by submitting the job to the Job Manager tool or executing it from the command line and then (v) finally, we analyze and inspect the obtained data by using the Nanoscope and the Result Browser tools.

Hence, VNL is designed to bridge experimental and computational approaches by offering a spectrum of useful tools for performing virtual experiments. The NanoLanguage scripts that are produced with VNL are performed with the ATK calculation engine. At any step in the work flow the user can export the simulation as a Python script, which can be executed by the command-line tool ATK python. This makes it easy to set up a calculation on a workstation but carry out the calculations on a cluster or more powerful computer. The result files can then be brought back to the workstation for analysis. All tools in VNL can also interpret Python code. This can be used to define a more complex geometry as a set of logical or repetitive operations in a script, which then directly can be used as input to the next step in the work flow. VNL is also extensible through user-defined plug-in components that can build special structures and perform specific analysis and plotting [71]. On the other hand, as is the case in most numerical simulations, a number of accuracy parameters must be specified to define the DFT and NEGF methods. Before we can study the electronic properties of a system, we first have to construct a model of the atomic

configuration we wish to investigate. VNL provides us with several tools that assist in defining the geometry of complex nanoscale systems [72].

Table 3.1: Summary of different usage stages of VNL toolbar during sample and device preparation and characterization.

Tool	Icon	Description
Molecular Builder		Build and construct our own molecules ready to be used in other VNL tools.
Atomic Manipulator		Set up two-probe systems and make modifications to magnetic tunnel junctions.
NanoLanguage Scripter		Create complete calculation set-ups and store these as Nano-Language script.
Method Editor		Predefine DFT and NEGF parameters for reuse in the Nano-Language Scripter when generating NanoLanguage scripts.
Script Editor		Manually edit and extend NanoLanguage scripts constructed by the different set of VNL tools.
Job Manager	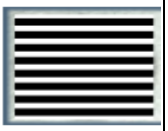	Execute scripts using the ATK computation engine.
Nanoscope		Visualize atomic geometries and calculated properties in 3D.

3.6 Sample Preparation

In the thesis work, we have prepared graphene nanoribbons of the width six parallel C –rows running along the length of the ribbon length of 10 unit repetitions. The

prepared samples edge doped either with hydrogen or oxygen, and then the glucose molecules are attached either in one side or in both sides of the ribbons with different concentration of the glucose.

The sample details are as follows,

(1) Zigzag GNRs of the specified widths and lengths are edge doped with hydrogen (H), and biomolecule is attached systematically either at one side or both sides of the ribbons. Thus a set of six samples are prepared and denoted by S1 to S6 sensor devices. Note that S1 device is devoid of any glucose.

(2) Zigzag GNRs of the specified widths and lengths are edge doped with oxygen (O), and biomolecule is attached systematically either at one sides or both sides of the ribbons. Thus another set of six samples are prepared and denoted by S'1 to S'6 sensor devices. Note that S'1 device is devoid of any glucose.

At first, we built glucose molecule in the molecular builder, the final optimized glucose is saved as the final adjusted glucose. Next, using python script we built a zigzag GNRs, which is dragged and dropped in the script editor where we specified the width and repetition of the as modeled produced zGNRs. Thus, the desired geometry, of zGNR's width of six and length is modeled repetition of ten. In second step we have passivated the edge of the zGNRs with hydrogen atom by using the molecular cupboard and produced the first category of sensors (S1 to S6). In the similar fashion we passivated the edge of the zGNRs with oxygen and produced the second category of sensors (S'1 to S'6). Accordingly we edge doped all the sensors with different concentration of glucose in a systematic manner. Where the concentration of glucose is ranged from 1 up to 6 with symmetric and asymmetric arrangements as described in the Table 3.2, and Table 3.3.

Table 3.2: Description of glucose Sensors of type I: the sensors have zGNRs edges terminated with hydrogen.

No	Sample name	Sensor	Configuration	Remarks
1	zGNR of width 6C-rows and length of 10 unit cells passivated with H	**S1**	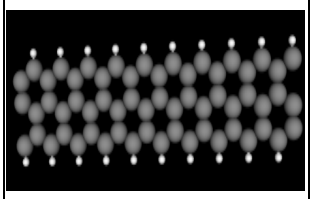	Without-effect of biomolecule
2	zGNR of width 6C-rows and length of 10 unit cells passivated with H	**S2**	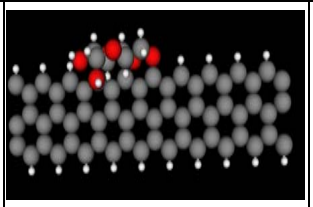	One-glucose molecule is attached at either side
3	zGNR of width 6C-rows and length of 10 unit cells passivated with H	**S3**	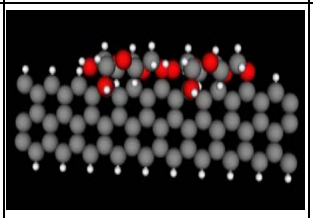	Two-glucose molecule is attached at either side
4	zGNR of width 6C-rows and length of 10 unit cells passivated with H	**S4**	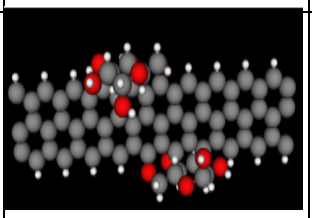	One-glucose molecule is attached to both side
5	zGNR of width 6C-rows and length of 10 unit cells passivated with H	**S5**	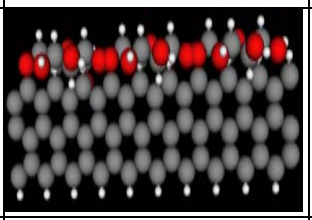	Three-glucose molecule is attached at either side
6	zGNR of width 6C-rows and length of 10 unit cells passivated with H	**S6**	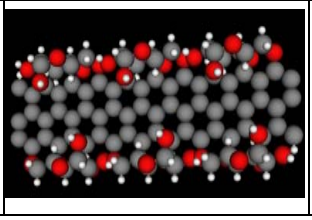	Three-glucose molecule is attached to both side

Table 3.3: Description of Glucose Sensors of type II: the sensors have zGNRs edges terminated with oxygen.

No	Sample name	Sensor	Configuration	Remarks
1	zGNR of width 6C-rows and length of 10 unit cells passivated with O	**S'1**	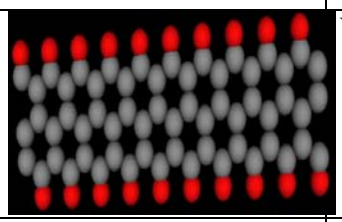	Without effect of biomolecule
2	zGNR of width 6C-rows and length of 10 unit cells passivated with O	**S'2**	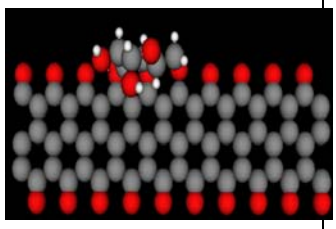	One-glucose molecule is attached at either side
3	zGNR of width 6C-rows and length of 10 unit cells passivated with O	**S'3**	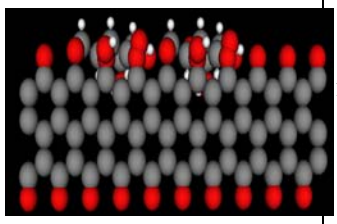	Two-glucose molecule is attached at either side
4	zGNR of width 6C-rows and length of 10 unit cells passivated with O	**S'4**	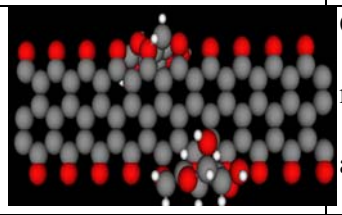	One-glucose molecule is attached at each side
5	zGNR of width 6C-rows and length of 10 unit cells passivated with O	**S'5**	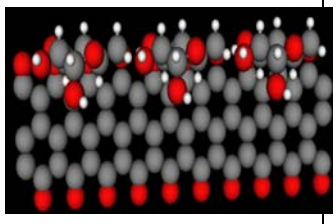	Three-glucose molecule is attached at either side
6	zGNR of width 6C-rows and length of 10 unit cells passivated with O	**S'6**	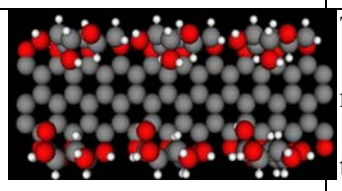	Three-glucose molecule is attached to each side

3.6.1 Two-Probe simulation device

The script of the sensor, from the atomic manipulator is dropped in the script editor. Here, the desired geometry with width six and repetition ten of zGNRs is set. In the second step, the modified python script for zGNRs is dragged and dropped in atomic manipulator where the device is cleaved to form two electrodes. In the third step, the samples I and II, are taken properly to build the central region of the system. The image and the script to build the two probe system saved as a separate file [72].

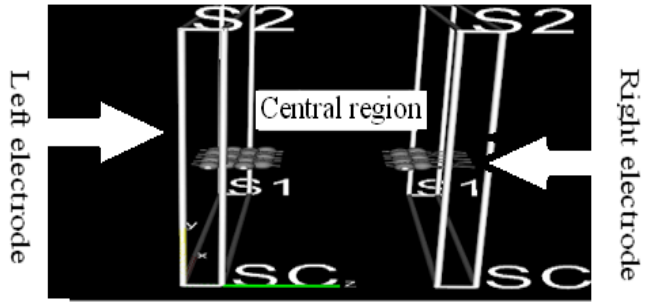

Figure 3.2: A schematic illustration of the two probe nanoribbon device. The connecting leads to central region are also made up of graphene nanoribbons.

3.6.2 Script preparation

The script which we saved in separate file dragged and dropped in NanoLanguage scripter to set the required parameters and all conditions in order to simulate Density of states (DOS), spectrum by fixing energy range of [-5, +5] in case of unbiased two probe system while along with these a parameter of current is added in case of biased two probe system. Here, Basis set with single zeta type is set under method tab. Also for biased two probe system electrode voltages are set across the left and right electrode in between -3 V to 3 V with an interval of 0.4 V for I–V characteristics,

while for unbiased two probe system the voltage on both electrodes is set 0 V. A numerical calculation (nc) file is created under the self consistent tab. Finally, under analysis tab we defined the quantities density of states (DOS). The path to store the calculated results is given and user modified python script is saved as a separate script.

Table 3.4: Basic Ab-initio Simulation parameters taken for DOS and I–V measurements.

Method Used	**Two probe Method**	
Basis Set parameters	Type	DZP
	Radial Sampling DR	0.001 Bohr
	Energy Shift	0.01 Rydberg
	Delta R (inner)	0.8
	V_0	40 Rydberg
	Charge	0
	Split Norm	0.15
	Element	All
Exchange Correlation Type	LDA.PZ	
Electron Density Parameters	Mesh Cutoff	150.00 Rydberg
Eigenstates occupation parameters	Electron temperature	300.0 K
Two Center Integral	Cutoff	2500.0 Rydberg

parameters	Number of points	1024
Iteration Mixing Parameters	Algorithm	Pulay
	Diagonal Mixing Parameter	0.1
	Quantity	Hamiltonian
	History Steps	6
Iteration Control Parameters	Tolerance	1e-005
	Criterion	Total Energy
	Max.Steps	500
Brillouin Zone Integration Parameters	Monkhorst Pack Parameters	(1,1,500)
Energy Zone Integration Parameters	Circle Points	30
	Integral Lower Bound Rydberg	3
	Fermi Function Poles	4
	Real Axis Infinitesimal Density	0.01 eV
	Real Axis Point Density	0.02 eV
Electrode Voltages	Voltage at Electrode 0	+1.00 V
	Voltage at Electrode 1	-1.00 V
Two Probe Algorithm Parameters	Electrode Constraint	Electrode Constraints 0ff
	Initial Density Type	Initial Density Type. Equivalent Bulk

3.6.3 Script Simulations

The saved modified python script for zGNRs of width 6-C rows and length of 10 unit cells either H or O-edge doped zGNRs attached with different concentrations of glucose is dragged and dropped in the job manager to carry out the simulation. i.e., to run the script and to calculate the desired results. As program execution terminated normally, a complete calculation file is obtained from the logout file and is stored for further analysis. This file consists of huge data as it includes the initialization parameters, user defined conditions, description about the nanostructure system and the coordinate values with respect to its dimensionality and most importantly the large iterative data of self consistent calculations. The basic idea behind the self consistent calculations is to calculate and compare the output values for the energies, obtained every successive iteration. This loop like process repeats continuously unless the difference between the two successive calculations becomes less than a default set value of accuracy. Once this state is attained the electron density gets converged and the energy minimized to attain the stability for the given nanostructure. The stored result from the .vnl file is dragged and dropped in the result browser or various plotter softwares like origin, to visualize the DOS plots in case of unbiased while to see the value of current along with these two for zGNRs based biased two probe system.Finally, the calculated data for DOS spectrum is obtained. Similarly, by extracting the value of current for each voltage combination on the electrodes the I-V characteristics for zGNRs based biased two probe system with different biased voltage are also plotted

CHAPTER FOUR

4 Results and Discussions

We have carried out the systematic first principle simulational studies for the electronic structure and transport properties on two different classes of sensor devices which are classified by the hydrogen or the oxygen edge doping of zigzag type graphene nanoribbons of finite width and length. Throughout this procedure of the sensor modeling, we have kept the fixed ribbon width with a value of 6C (six carbons) rows and the length is also fixed by 10 unit cells to minimize any sensing variations that arise from the changes induced by the geometric shape alterations. Following this the electronic structures and transport properties from the ribbon are studied. The results and discussions are organized by first discussing the simulated density of states at zero bias for the hydrogen edge-doped ribbons with various concentrations of glucose molecule attachments to the ribbon edge. We have concentrated most of our discussion around the low energy electrons that are the Dirac-fermions as discussed earlier in the introductory part and owing to the vital role played by them in the device sensing. These studies are further preceded by effects of gating through a connection of third electrode to the sensor device, which supplies both the positive and the negative kind of biases to the ribbon under the influence of the glucose environment. These studies are conclusively completed by the comparison of the sensing behavior obtained from the I-V measurements for a set of six sensor devices under the influence of varying concentrations of glucose environments. A similar set of studies are also performed for the type II sensors (S'1 to S'6) having oxygen edge doped ribbons at the central region. In the end we have also attempted to differentiate in between the performance of H-edge doped sensors and O-edge doped glucose sensors.

4.1 Glucose Concentration dependent DOS in H-doped zGNRs

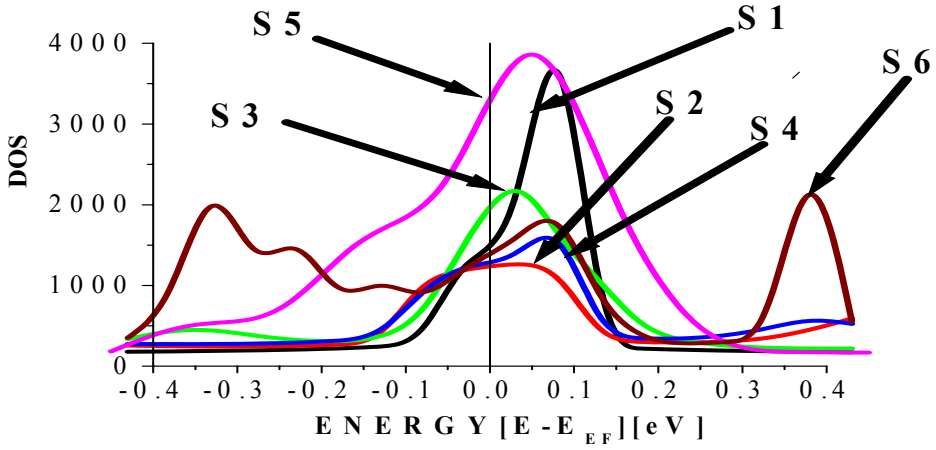

Figure 4.1: DOS spectrum of six H-edge doped ribbon sensors (S1 to S6) without gate bias. Note that the symbols S1 to S6 have their usual meaning as described in the sample synthesis part (Table 3.2) in the Chapter 3.

A Figure 4.1 shows the DOS spectra of the six sensor devices with and without glucose attachments. As the sensor is meant for operations at low voltages hence a high resolution spectra is recorded at a small spectra energy step size of 20 meV. The hydrogenated nanoribbon which is devoid of any biomolecular attachments shows a total energy minimum of -13596.02 eV which indicates a higher stability of as prepared theoretical sensor devices. The self consistent calculations yield a significant value of charge transfer at the central region of the sensors from its electrodes. Before starting the calculations we have observed that the total amount of initial charge on active region of the sensor is of the value of 312.000 e, where e = 1.602 $x10^{-19}$ C. After attaining the self consistency it is found that the charge on the region gets slightly increased to 312.017 e. As the charge on the central region is increased, it is expected that the electron related a charge scattering should increased. We have plotted the DOS spectra in the Figure 4.1 such that the Fermi level value which is

obtained as a negative value in all of our calculation is subtracted from the band structure energy values of the calculation; hence, for the right of the zero point in the DOS, the states for negative carriers are visible. Similarly, on the left of the zero point we have the states for holes. Therefore it is expected that the slight increase of charge in the central region will disturb the resonant states at Fermi level. Earlier also, it has been observed by several researchers that the zGNR when placed in the two probe devices show reduced metallicity due to the pinned out equilibrium states [72].

Table 4.1: Results summary of E_{TOTAL} (eV) at zero gate bias for H-edge doped zGNRs.

Sensor	**E_{TOTAL} (eV)**
S1	-13596.02
S2	-17215.81
S3	-20792.36
S4	-20855.69
S5	-24367.34
S6	-35205.69

In our expexperiments we have observed a significant reduction in the states of H-zGNRs in the device which are nearly ~2200 as compared to several tens of thousand states present in the similar energy window for the pristine zGNRs. At the same time we have also found some resonant peaks adjacent to the contributing states on the right hand side of the DOS spectra (S1). Because of the said charge admittance one can expect such peaks on the DOS spectra owing to the electron related resonant states along with the Fermi pinned out electronic states centered at the 100 meV. In

the sensor S1, the charge transfer from electrodes is found to be +0.017 e, the positive sign means that the increased electron scattering should reduces the available contributing states of the ribbon in the device in comparison to that of isolated one. Obviously, this nature of the charge carriers also manifests in the form of unpinned Fermi peak of this device. Next, among the sensors S2 to S6, those are attached by the glucose molecule, none of them show charge admittance from the electrodes. Hence we have a clear resonance signature amidst the equilibrium states, especially in the sample S5 that shows large value of 4000 states at the zero point. At the same time in all of these samples we got the symmetric distribution of equilibrium states indicating the pinning of the states. The electrode charge admittance also increases by the negative values of -0.316 e, -0.591 e, -0.543 e, -0.845 e, and -1.594 e for the devices S2, S3, S4, S5, and S6, respectively. Another prominent observation is that as the charge admittance increases, the zero point equilibrium states are found to exhibit a systematic decrease in the peak intensities and all the devices show corresponding decremental states that are clearly evident from the as shown DOS spectra of Figure 4.1. The peak intensity at zero point is minimum for the sensor S6 that is attached by six biomolecular entities and for which the charge admittance is increased by 1.611 e in comparison to that of the pristine one which is about +0.017 e. But due to the higher stability of S4 in comparison to S3 due to lower energy formation as given in the Table 4.1, we have less charge admittance which is an exceptional outcome. At the same time we have also observed a biomolecular charge remittance, which is in general found to decrease with glucose concentration with the values of -4.935 e, -4.235 e, -4.555 e, +4.451 e, and +6.312 e, respectively. But again due to the higher stability of sensor S4 in comparison to S3 we have more biomolecular remittance in S4 than in S3. Observance of the maximum equilibrium DOS for the sensor S5 with

the value of 4000 and minimum for S6 device accompanied by two small peaks on either sides of Fermi level arise due to two parallel competing processes of the charge transfer by central region to electrodes and the admittance from the bimolecular attachment giving rise to low energy spectral positions of these two peaks at -0.329 me V and +0.379 me V, respectively. It is to be noted that in the samples S5 and S6 we have positive charge remittance.

4.2 Gating effects on H-doped zGNRs

For the sample S1 which is devoid of any biomolecular attachments we observed that at the application of gate the value of equilibrium states increases to around 1590 and there is an increment of almost 90 on its DOS spectra as shown in Figure 4.2 (a). This clearly shows the further Fermi pinning of resonant states with gating. Also, the unbiased peak maxima spectral position for this sensor is observed before gating at +0.379 eV. Such Fermi pinning of the device can be explained by the large charge admittance to the electrodes, as we can see the admittance values are -0.622 e, -1.299 e, and -1.998 e for +1 V, +2 V, and +3 V, gate bias respectively. However, the increasing trends of electron transfer in between the electrodes and the central region are also associated with the decrease in the equilibrium states from +1 V to +3 V due to the increased charge scattering in the central region. For the negative voltages particularly, we do not observe any Fermi unpinning even though the charge admittance values are +0.558 e, and ,+0.688 e for gate bias voltage -1 V, and -2 V respectively and the equilibrium state peak is found to be narrower in the later case. Also no other significant peaks are observable in the near vicinity of the zero point, which is a position of the Fermi level in our Fermi energy correction spectra. We also found that the DOS peak become narrow with the application of negative gate bias.

From our results we attribute the observed change in the DOS to the charge transfer in between the central region and the electrodes of the nanodevices. Hence there is a significant amount of charge transfer in the sensor S1 at various gate biases that is accompanied with a strong coupling among various regions of the device. Hence the central region would have lesser amount of charge scattering, which is also visible from the broader DOS peak at the zero point of these devices.

The equilibrium contributing states for S2 device which is attached with one glucose molecule is found to be around 7000 without any bowing on either side of zero point energy as shown in the Figure 4.2 (b), the total energy at zero bias is -17215.81 eV. However, with the application of gate bias a significant amount of change in equilibrium conductance is observed. For gate voltage of +1 V there is a distortion in the central DOS peak and this is a clear Fermi unpinning on the positive side of zero point is observed. Similarly, at negative voltage of -3 V the device shows prominent reduction in contributing states. This could be due to anti-resonance nature of fano like coupling in between the central region and electrodes with exceptionally high value of charge transfer of 2.900 e to the electrodes.

The similar kind of destruction in the contributing states is also observed in the density of states, Figure 4.2 (c), for the device S3 that is attached with two glucose molecules at the gate bias of -3 V. Also we have found that at the negative gate bias voltages the self consistent calculation for this sensor (S2) consumes longer time for subsequent iterative runs, which could be due to as introduced unstability in charge transfer by this type of coupling. On the basis of these results in general we found that the strength of this particular coupling increases with the negative gate bias, and always accompanied by the higher values of self consistent iterations the successful termination of the DFT code. Normally, we found that this effect is more like a device

specific trait and less dependent on the chemical environment like a glucose molecule attachment. In addition to this, with the application of higher negative voltages we found that in general the device stability, decreases for instance at zero gate bias the stability of S2 and S3 devices are -17215.81 eV, and -20792.36 eV, but at gate voltage of -3 V the stability is reduced with the values of -16952.78 eV ,and -20529.05 eV, respectively.

Hence, we ascribed the reason of large calculation times to the as discussed device instabilities at higher negative gate bias. The charge transfer at +1 V, +2 V, and +3 V are -0.957 e, -1.642 e and -2.350 e, respectively. In similar analogy to the previous device, here also, we have decrease in resonant states with noticeable amount of charge transfer along with the Fermi pinning, clearly the as observed positive bowing is maximum in the +1 V gate bias. At the same time there is a charge admittance in the attached glucose molecules which further reduces the charge scattering and increases in the DOS. The two processes are competing due to already explained reasons before for the sensor S1. The charge transfer to glucose decreases with increase in the positive bias. For other gate bias voltages of -3 V we observed the charge transfer from electrodes to central region of -2.900 e, and charge admittance of -5.120 e in the bimolecular attachment, we found minimum DOS for this sample with bowing of equilibrium states in negative energies. But for the other gate bias of -1 V we observed an additional peak on the positive side of Fermi energy at 0.3 eV due to positive charge transfer of +0.222 e from electrodes to the central region which has manifested in the form of this resonant state. For all the other gate biases we didn't find any significant variation in equilibrium states.

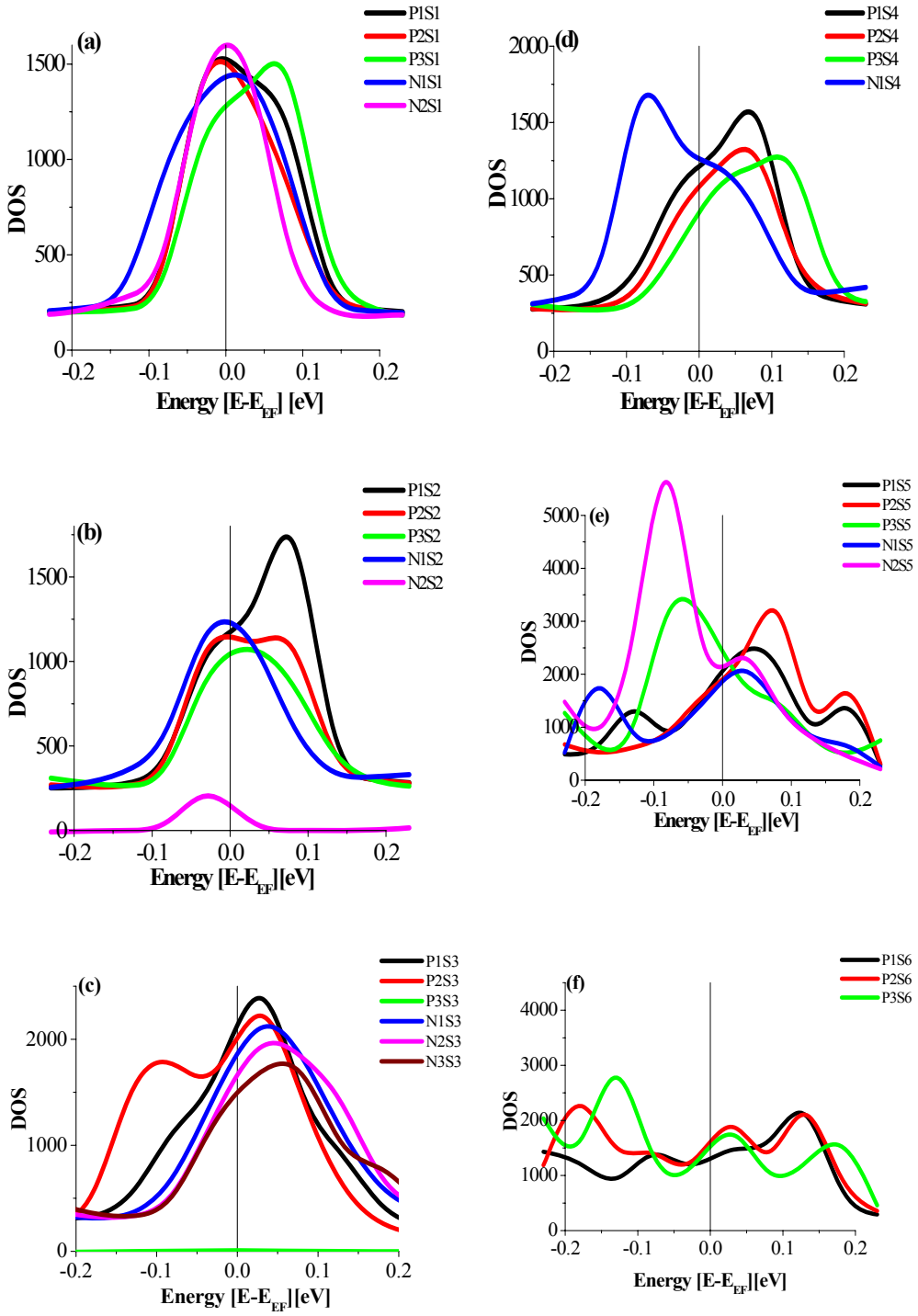

Figure 4.2: DOS Spectrum of six H-terminated sensors (S1 to S6) with gate bias in between the range of ±3 V are shown in the Figure (a) to (f) respectively.

Table 4.2: Results summary of E_{TOTAL} (eV) with gate bias for H-edge doped zGNRs.

Sensor	Gate (V)	E_{TOTAL} (eV)	Sensor	Gate (V)	E_{TOTAL} (eV)
S1	+3	-13584.99	S4	+3	-20843.64
	+2	-13589.68		+2	-20848.52
	+1	-13593.60		+1	-20852.60
	-1	-13598.09		-1	-20857.23
	-2	-13594.91	S5	+3	-24355.28
S2	+3	-17204.01		+2	-24360.17
	+2	-17208.7		+1	-24364.25
	+1	-17212.78		-1	-24368.99
	-1	-17217.36		-2	-24367.05
	-3	-16952.78	S6	+3	-35193.37
S3	+3	-20780.43		+2	-35198.39
	+2	-20785.25		+1	-35202.53
	+1	-20789.30			
	-1	-20793.89			
	-2	-20790.49			
	-3	-20529.05			

The sensor S3 has two glucose molecules unequally distributed such that only one side of ribbon is exposed with glucose attachment hence both zigzag sides of the ribbon undoubtedly have different chemical environment, on the contrary the sensor

S4 also have two glucose molecules attachment but with equal distribution on either side of the ribbon. If we compare these two sensors, the stability is found to be more in S4 device with total energy value of -20855.69 eV, while the total energy value of S3 device having similar number of chemical entities is -20792.36 eV, which is a significant variation in stabilities. This gated device S3 is thus insulative for low energy electrons, which is also evident from zero contributing states at bias of -3 V, here also the charge transfer from central region to electrodes is high with -2.989 e. However, the charge acceptance of glucose is increased by the value of -4.636 e in comparison to other values of -4.546 e and -5.018 e for -2 V, and -1 V respectively. Depending upon the high value of charge transfer to electrodes we got a highly shifted equilibrium resonant states at nearly -0.5 V. For one of the gate bias of -2V, we found a charge acceptance of +0.134 e and owing to this fact the resonant states peak is shifted near to zero point at -100 meV. For positive gate biases we do not observe any significant deviation from the zero bias traits of positive bowing. Also in the device S3 we mostly have narrow peaks of contributing states at positive voltages, centering around DOS value of 2000 with high charge transfer values, the charge transfer at +1 V, +2 V and +3 V is -4.077 e, -3.920 e, and -3.763 e, respectively. In general, we observed that the increase in charge transfer to glucose decreases the intensities of the DOS peaks on the positive sides of the Fermi point.

In the device S4 for the gate voltages + 1 V ,+2 V ,+3 V, and -1 V ,we have obtained a large number equilibrium states which are almost comparable to that of without gate application, however it should be noted that at zero gate bias of S4 devices the peak maxima is situated more on positive side of zero point, but with -1 V gate bias we have an exceptional bowing of central peaks for low negative energies indicative of the change in nature of the free carrier types. Again we ascribed this effect to the

presence of ribbons charge admittance of +0.003 e from electrodes to the central regions. On comparing with positive gate biases we have found that in all cases a charge transfer phenomena from central region to electrodes and it is manifested in the form of bowing of the equilibrium peak for positive energies. Nonetheless, the bowing is maximum for +3 V gate voltages where the charge transfer is -2.612 e.

In the device S5 the three glucose molecules are attached on the same side of the ribbon hence the chemical environment is very different for the two sides of the zGNRs, this is the device which also shows maximum density of states near the zero point but not exactly in equilibrium and slightly away by -100 meV from the zero point at -2 V gate bias. In this device for positive gate bias we consistently obtained higher values of charge transfer to electrodes, for instance the values are -1.547 e, -2.284 e, and -3.055 e, hence the values of equilibrium peaks are always small in comparison to that for negative bias. It is to be noted that we obtained flipping of charge admittance by increasing gate bias from -1 V to -2 V because charge transfer changes from -0.229 e to +1.306 e. This effect manifest itself in the form of large resonant state peak just below the Fermi level as described before. Also we found that the glucose molecule starts remitting the charge back to central region once the concentration of glucose increases. Evidently, the charge remittance from glucose increases on increasing the positive gate biases for the three biomolecule attachment with this sensor device. It increases from +4.682 e to +5.143 e from +1 V to +3 V. Charge remittance decreases slightly from -1 V to -2 V by value of nearly 0.230 e.

In the device S6 both the side edges are under similar chemical environment and here we observed two new peaks along with central peak for low energy charge carriers without any gating of the device, the total energy for this device is -35205.67 eV which the lowest minima amongst all of the other devices. Thus as expected the

electrodes coupling should be the strongest owing to this maximum stability. This fact is also manifested from the charge transfer that is maximum in this device from central region to electrodes with the value of -1.595 e which can be responsible for evolution of peak at lower end of zero point. Similarly, the device exhibits high charge transfer from glucose to ribbon as 69.98 e that is the charge accumulated per glucose molecule is still high and manifested in the form of peak at upper side of zero point. With the application of positive gate bias we can see from Figure 4.2 (f) that lower energy contributing states show a usual favor for hole conduction, even at bias of +3 V and there is a complete absence of previous peak for electron contributing states at the upper end of the zero point.

4.3 I–V Characteristics of H-doped zGNRs Glucose Sensor

In general the sensor without glucose attachment shows linear I–V dependence as shown in Figure 4.3 (S1), but with biomolecule attachment a phenomenon of non ohmcity manifests in the form of non-linear I–V curves. Also the extent of non linearity increases with glucose concentration such that some times a negative differential resistance is also observed from I–V measurements. From the previous DOS results we know that the pure hydrogen passivated material do not have singularities arising from the dangling states as the GNRs material is passivated by hydrogen, as a result no sharp DOS observed, but when the zGNRs passivated with hydrogen are doped with different concentration of glucose the sharp peaks are observed depending on the concentration of the glucose. Thus in the pure zGNRs which are passivated by hydrogen both NDR (negative differential resistance) and conductance oscillations are not observed. But when the ribbons doped with glucose of different concentration, the NDR and the conductance oscillations are appeared.

Furthermore, it is found that the oscillations are small in magnitude when the glucose concentration is low and gradually increase with higher glucose concentrations.

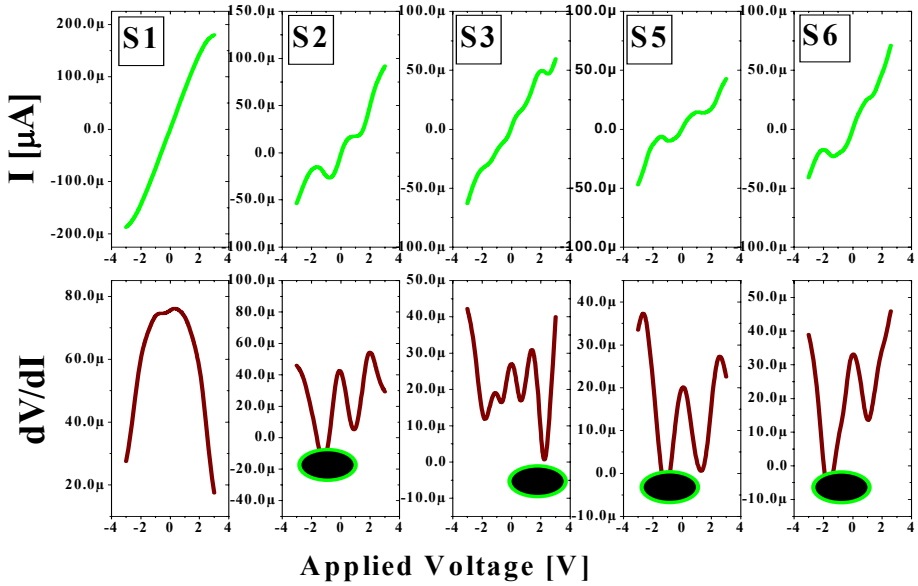

Figure 4.3: Simulated I–V results of H edge doped zGNRs glucose sensors at source-drain bias of ±3 V, with the bias step size of 0.4 V. All the measurements are performed at zero gate bias by keeping V_g= 0 V.The glucose concentration varies in sensors from S1 to S6 with its usual connotations.

In general, it is found that the current decreases from devices S2-S3-S5, which is also corroborated from DOS spectrum; the width of peak at Fermi level which decreases from S2-S3-S5. Nevertheless, for S6 there is a presence of a lot of closely spaced singularities in DOS which results in conduction centributing around Fermi energy, and this helps in increasing the current maxima of the device S6 in respect to S5. In conclusion these sensors of type I (sensors edge doped with hydrogen) show a decreasing current proportional to increase in glucose concentration provided that we should cover up one complete side of GNR by some suitable encapsulation. Thus these sensors are very efficient, because always in presence of glucose, they start

showing negative differential resistance with systematic variation in the current maxima, which is a sort of qualitative sensing, Hence, using these sensors with one side encapsulation can easily perform both qualitative and quantitative analysis of glucose concentrations in any given medium.

4.4 Glucose concentration dependent DOS in O-doped zGNRs

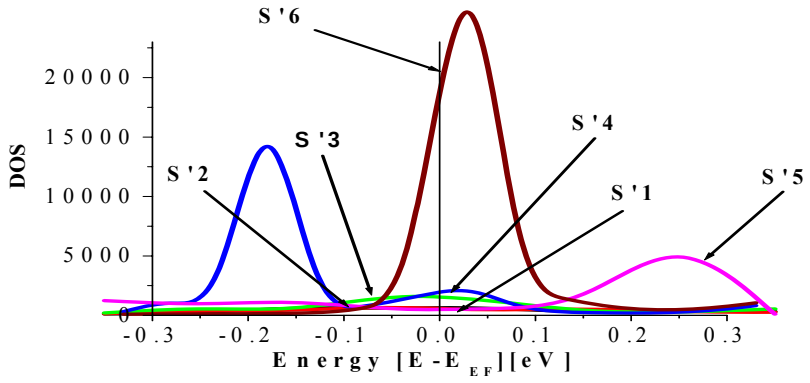

Figure 4.4: DOS of six O-edge doped ribbon sensors (S'1 to S'6) without gate bias. Note that the symbols S'1 to S'6 have their usual meaning as described in the sample synthesis part (Table 3.3) in Chapter 3.

In this section we will discuss about the ribbons which are terminated by oxygen atoms at their two edges and their used in glucose sensing. For the oxygen doped glucose sensors also the charge admittance of the sensor electrodes increases with the concentration of glucose around the central zGNRs region, we observed the charge in net admittance from +0.817 e to -1.012 e from bare ribbon (S'1) to the ribbon attached with six glucose molecules. Without gate biasing the oxygenated devices show some very strange artifacts in the presence of glucose and also these effects are found to be glucose concentration dependent. The DOS spectra of oxygenated ribbon without any glucose attachment show negligible contributing states at the Fermi position.

Typically, we obtained high equilibrium states which increases with the glucose attachment. For instance, sample S'6 with six glucose molecule attachment on both sides of the ribbon shows metallic graphene like behaviour with nearly thirty thousands states at zero point and incomparision the pristine bare ribbon shows just 500 states at the same spectral position.

Table 4.3: Results summary of E_{TOTAL} (eV) at zero gate bias for O-edge doped zGNRs

Sensor	**E_{TOTAL}(eV)**
S'1	-21856.35
S'2	-24988.54
S'3	-28233.79
S'4	-28233.77
S'5	-31244.09
S'6	-40999.26

The reason is that the oxygen atom is highly electronegative in comparison to the previous H-passivents, thus it accepts and distorts the pi-electron cloud overlapping of the zigzag edges which are mainly responsible for the ribbon conductivities. Hence because of the passivent related band gap opening charge exchange with electrodes we observed such huge states in this device. But the sample S'5 is an exception in which Fermi energy level is pinned out by 250 meV on right side of zero point. In this sample the effect of biomolecule attached on only one side of ribbon is similar to the effect of gating, in that also the Fermi unpinning is frequent. Also we have found that the glucose charge admittance deceases with concentration in case of oxygen doped

ribbon, but it never remits back the charge to the central region. It is to be noted that the similar charge remittance from glucose is observed before in hydrogen doped ribbons. As a result we got lower minima for all O-doped sensors irrespective of gating which makes them highly stable. The energy minima for samples S'1 to S'6 is found to be -21856.35eV, -24988.54 eV, -28233.79 eV, -28233.79 eV, -31244.09 eV, and -40999.26 eV respectively. Without any glucose/biomolecule attachment, the as prepared sensor devices (S'1) has the total energy of -21856.35 eV, and on attaching glucose molecules the energy minima increases upto -40999.26 eV for six glucose attachment to oxygenated ribbon. Because of the higher stability in O-doped system we do not observe any change of energy minima in respect to the change of asymmetric to symmetric conformations among the samples S'3 and S'4.

4.5 Gating Effects on O-doped zGNRs

We obtained small number of equilibrium states in S'1 due to as discussed weak pi-conduction channels on ribbon edges, but we have observed a pinned out peak at negative side of Fermi position at -250 meV for all gate biases. Also there is no significant electron conduction resonant state on the right hand side of the DOS spectrum. The order of charge remittance from central region to the electrodes increases with gate bias in this no glucose molecule sensor, which increases from +1 V, +2 V, and, +3 V by the remittance values of -0.292 e, -1.034 e, and -1.786 e, this can be explained by the fact that electron scattering lower down by decrease in the net accumulated charge and hence the resonant state at zero point are observed. On the contrary for the negative biases the equilibrium states increases with charge admittance. Similarly, the device S'2 which has one glucose attachment do not show any significant number of equilibrium states, but amongst the S'3, and S'4 devices

we observe a higher number of states just below the Fermi position in S'4. It is to be noted that higher charge transfer of 2.615 e takes place from the glucose to the central region in S'4 in comparison to 1.815 e for that of S'3 device, while a charge transfer from electrodes to central regions of both of these devices is exactly equal to 0.1434 e, and thus its net positive value implies that the scattering for electrons should increased in the central region.

In device S'3 there is a maximum charge transfer in gate bias of +3 V which comprises of -2.162 e charge transfer value from the central region to the electrodes. While for +2 V, and +1 V the charge transfer values are -0.666e, and -1.407 e. Hence due to increased charge scattering and lesser resonant tunneling states, the equilibrium conductance decreases on increasing on the positive bias as clearly depicted from the DOS spectra of Figure 4.5 (c) for the sample at the spectrum position of zero point. The equilibrium is maximum for +1 V that is also the usual case for previously discussed sensors with the application of positive biases. At the same time the charge admittance of glucose molecule decreases with the small value of nearly 1.6 e on increasing the bias upto +3 V, which also contribute to the as obtained less equilibrium conductance values. For the negative bias the charge acceptance in the central region increases from +0.680 e to +1.046 e for -1 V, and -2 V, respectively, and the charge admittance to glucose increases slightly by 0.1 e. If we look at the DOS spectra in Figure 4.5 (c) for negative biases the equilibrium conductance decreases with charge remittance from electrodes to the central regions. Also for -1 V gate bias an intense DOS peak at the upper vicinity of Fermi level is evolved with almost twenty thousands states positioned at 200 meV, which contribute towards the electron transmittance from the sensor. Similarly, in the lower bound of Fermi level, a

DOS peak appears at -2 V gate bias with twelve thousands states positioned at -200 meV, it can be ascribed to contribute hole transmittance.

In the S'4 device, it is found that the charge transfer increases with positive potential on gate bias from the initial value of -0.584 e for +1 V to -2.114 e for +3 V gatings. Exceptionally, in this case the conductance slightly increases with the gate bias, indicating a kind of oscillatory conductance to charge transfer pattern [72]. As discussed before in the Chapter 1 the charge transfer brings a natural evolution of LUMO or HOMO levels of the central nanocrystalline region and induces their alignment with the Fermi level of the electrodes, manifesting in the form of equilibrium conductance.

Earlier also it has been reported that the effect of charge transfer is oscillatory on the conductance of the device [73], and also the effects of charge transfer is found to fill and bring the broadening in LUMO or HOMO levels to further facilitate the Fermi level alignment with electrodes and these states are found to contribute significantly to conduction [74]. Gating of -1 V and -2 V in this device bring the charge transfer values are -0.584 e and +1.108 e from electrodes to the central region, here also the conductance is expected to be more for the higher gate biases.

In the device S'5 although the charge transfer to electrodes monotonically increases from the values of -0.919 e, -1.681 e, and -2.459 e for +1 V, +2 V, and +3 V respectively as shown in the Figure 4.5 (e). Nevertheless, the maximum equilibrium conducting states are obtained at +2 V which again indicates the oscillatory dependence of LUMO-HOMO alignment with the charge transfer in the sensor S'4.

Finally, the sensor S'6 shows linear dependence of charge transfer to equilibrium conductance as evident from the results of the DOS spectra in Figure 4.5 (f), which show the charge transfer of -1.813 e, -2.638 e , and -3.478 e, for +1 V,+2 V, and

+3 V, respectively and conductance decreases accordingly. As this is the sample with maximum number of glucose molecules and shows highest value of charge transfer at +1 V in comparison to other sensors thus the maximum equilibrium conducting states are around ten thousand in number.

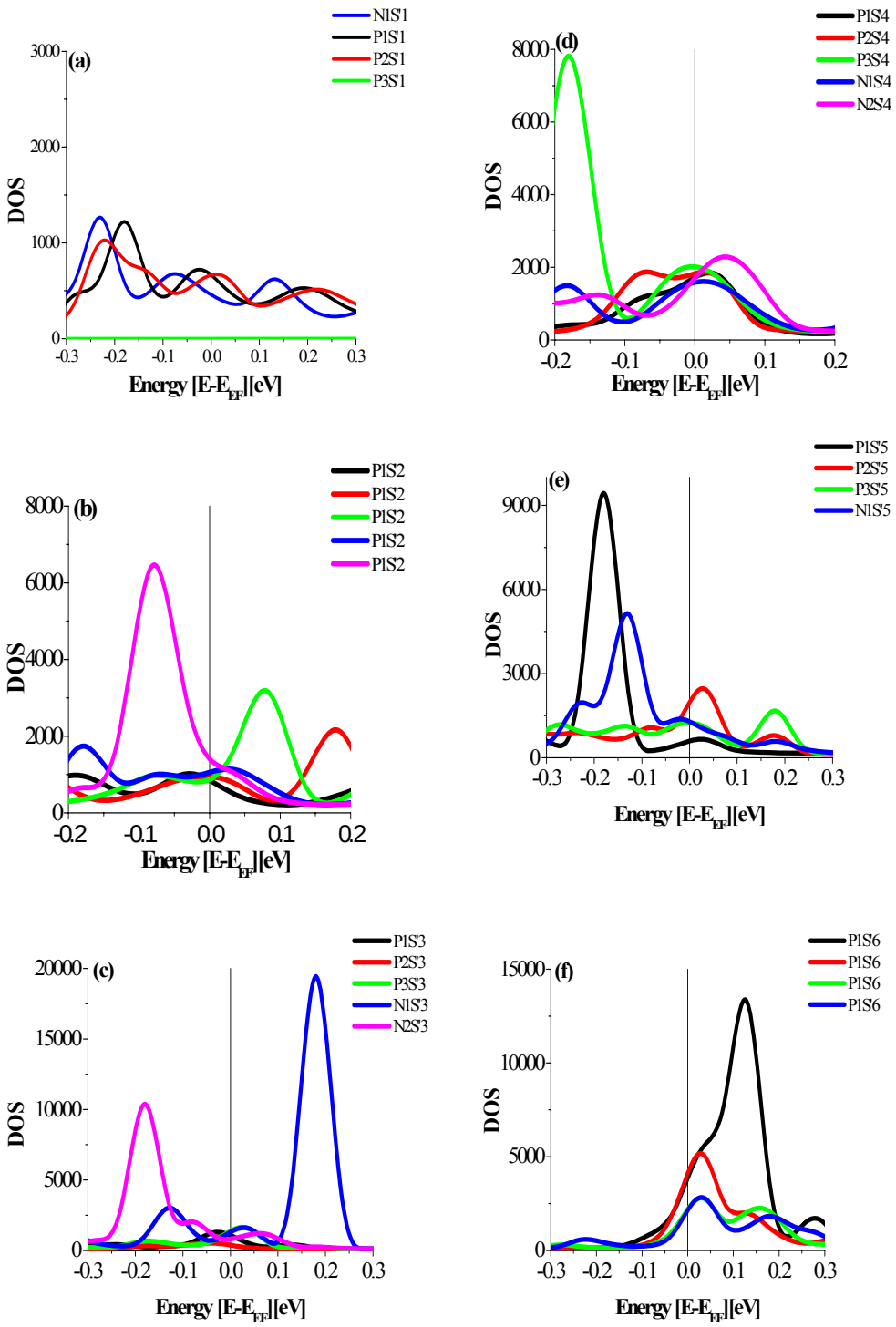

Figure 4.5: DOS spectrum of six sensors (S'1 to S'6) with gate bias in between the rang of ±3 V are shown in the Figures (a) to (f) respectively.

Table 4.4: Results summary of E_{TOTAL} (eV) with gate bias for O-edge doped zGNRs

Sensor	Gate (V)	E_{TOTAL} (eV)	Sensor	Gate (V)	E_{TOTAL} (eV)
S'1	+3	-21846.38	S'4	+3	-28223.01
	+2	-21850.53		+2	-28227.50
	+1	-21853.89		+1	-28231.13
	-1	-21857.66		-1	-28235.18
				-2	-28115.99
S'2	+3	-24978.31	S'5	+3	-31233.16
	+2	-24982.57		+2	-31237.63
	+1	-24986.02		+1	-31241.29
	-1	-24989.88		-1	-31245.77
	-2	-24988.89	S'6	+3	-40987.24
S'3	+3	-28106.59		+2	-40992.19
	+2	-28110.92		+1	-40996.25
	+1	-28114.43		-1	-41000.89
	-1	-28118.35			
	-2	-28115.99			

4.6 I–V Characteristics of O-edge doped zGNRs Glucose Sensor

In general the sensor without glucose attachment shows linear I–V dependence as shown by I–V of sample S'1 in the Figure 4.6, but with biomolecule attachment non ohmcity manifests in the form of non-linear I–V curves. Also the non-linearity increases with glucose concentration in O-zGNRs we have never observed the negative differential resistance. Pure oxygen passivated material do not show singularity because of dangling states are passivated by oxygen, as a result no sharp DOS peak is observed, but when the zGNRs passivated with oxygen doped with different concentrations of glucose the sharp peaks are observed depending on the corresponding concentrations. In pure zGNRs which is passivated by oxygen, both NDR (negative differential resistance) and conductance oscillations are not observed. But when the ribbons edge is attached with glucose of different concentrations the nonlinearity is greatly enhanced without any NDR or conductance oscillations. Furthermore, the extent of rectifying nature is small when glucose concentration is low; in contrast nonlinearity increases with glucose concentration. Current decreases from S'1 to S'2 and from S'2 to S'5, which is evident from the spectra of width of the peak at Fermi level which decreases from S'1 to S'2 and S'3 to S'5. In conclusion, our O-zGNRs sensors exhibit a rectifying current plateau, with the attachment of glucose molecule to the ribbon, and the width of current plateau is found to be systematically dependent on the concentration of glucose. As evident from the Figure 4.6 (S'2) and 4.6 (S'5), it is clear that the plateau width is small around 2.5 V for low glucose concentration of 1 molecule. But as the glucose concentration increases to 3 molecules for S'5 device, we can see that the plateau width gets increased to ~ 4.0 V,

which is strong signature for the capability of single molecular sensing from our proposed sensor architecture.

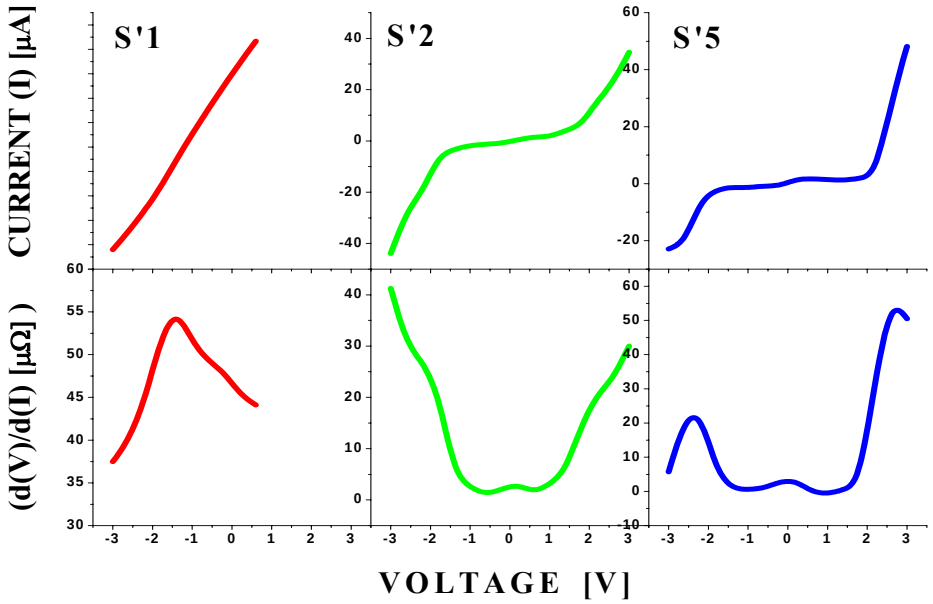

Figure 4.6: Simulated I–V results of O-edge doped zGNRs glucose sensors at source-drain bias of ±3 V, with the bias step-size of 0.4 V. All the measurement are performed at zero gate bias by keeping V_g= 0 V.The glucose concentration varies in sensors from S'1 to S'6 with its usual connotations. The lower pencil depicts the results of differential resistance.

CHAPTER FIVE

5 Conclusions and Future Outlooks

5.1 Conclusions

We have performed a systematic ab-initio DFT-LDA based modeling of the graphene nanoribbon sensors and successfully performed the study of sensor performance in the presence of glucose environments. We have found that the modeled sensors made up of the hydrogen and oxygen edge doped stable nanoribbons are suitable for deployment for the single molecule sensing. These ultra responsive sensors are tested for even one, two and three glucose molecular attachments. Firstly, the molecules are attached on one side of the ribbon followed by both sides. Even for the equal glucoses concentrations we have found that the sensor response is different due to the presence of enveloping side of the ribbon. This effect is ascribed to the availability of full π-conduction channel on the enveloped zigzag edge of the H-doped ribbon and also due to asymmetry related changes in the total energies of the two devices. Nevertheless, among the O-doped sensors, such trends are found to be missing and the total energies for symmetric and asymmetric glucose attachments are found to be comparable. We have found that the sensors exhibit significant variations in equilibrium conductance around the zero point of the DOS and at the Fermi level with the increasing glucose concentrations. Finally on the basis of the trends obtained from the electronic and transport phenomena we have presented and discussed our sensors I–V behavior in the presence of the varying glucose concentrations. Without the attachment of the glucose or any biomolecular attachment in general we found that the I–V behavior shows the linearity and ohmic characteristics in both the sensing systems of H-GNRs and O-GNRs. However the nonlinearity comes into play with the biomolecular

attachments. Specifically we have found certain features which indicate the presence of the glucose in the vicinity of the ribbon and the concentration dependency of the glucose, in the light of novel phenomenon of NDR and the quantum size effect induced nonlinearities. The H graphene ribbon shows negative differential resistances when attached by the glucose molecules. And the current maxima and the spectral position of the NDR regimes is mostly found to be concentration dependent. Hence for both qualitative glucose sensing as well as its quantization with respect varying concentration is found to be feasible in the one side encapsulated graphene sensors. In the O-graphene ribbon it has been concluded that the NDR is absent in all the sensors which can be ascribed to the high level of as found stability in the O-doping. Nevertheless, the presence of glucose in its increasing concentration is very well described by the newly discovered non-linearities from the present set of simulational experiments. We found the non-linearity increase and in particular, the current less window width that becomes more flatter and plateau like at higher glucose concentrations. It is needless to say that from our results on glucose sensors made up of doped graphene ribbons, a new field of single molecular sensing opens up which will pave the way for availability of highly portable and more responsive medical sensors than currently available commercial products.

5.2 Future outlooks

Although we have already performed a much-detailed studies on the response of glucose environment to nanoribbons transport behavior. The response of presence of ketones, higher level sugars and other organic ring compounds in the animal blood and their inferences on the glucose sensing is still an open meadow for research.

References:

1 Pauling L., The Nature of the Chemical Bond, Cornell University Press, Ithaca NY, (1960) 686

2 Yan QM, Huang B, Yu J, Zheng FW, Zang J, Wu J, Gu BL, Liu F, Duan WH. Nano Lett. 7 (2007) 1473

3 URL: http://www.childrenwithdiabetes.com Retrieved on March, 9, (2012)

4 URL: http://www.glucowatch.com , Retrieved on March, 17, (2012)

5 URL: http://www.agsci.ubs.ca. Retrieved on March, 17, (2012)

6 URL:http://www.clinicip.org/index.php.id=242 , Retrieved on March, 17, (2012)

7 URL: http://www.betachek.com/bv.htm Retrieved on March,17, (2012)

8 Katsnelson MI. Materials Today 10 (2007) 27

9 Curl RL. Rev. Mod. Phys 69 (1997) 703

10 Kroto H. Rev. Mod. Phys. 69 (1997) 722

11 Iijima S. Nature 54 (1991) 166804

12 Geim AK and Novoselov KS. Nat. Mater. 6 (2007) 183

13 Changyao C, Sami R, Kirill IB, William K, Philip K, Ioannis K, Horst LS, Tony FH, James H. Nature Nanotechnology 4 (2009) 867

14 Lee XW, Kysar JW, Hone J. Science 321 (2008) 388

15 Wallace PR. Phys. Rev. 71 (1947) 634

16 Heersche HB, Jarillo-Herrero P, Oostinga JB, Vandersypen LM. Matter Nature 446 (2007) 59

17 Peres NR, Guinea F, Castro Neto AH. Phys. Rev. B, 73 (2006) 125411

18 Novoselov KS, Jiang D, Shedin F, Boothand TJ, Khotkevich V, Morozov SV, Geim AK. Proc. Natl Acad. Sci. USA, 102 (2005) 10451

19 Martins TB, Miwa RH, Antonio JRS, Fazzio A. Phys. Rev. Lett. 98 (2007) 196803

20 Geim AK and Novoselov KS. Nat. Mater, 6 (2007) 750

21 Booth TJ, Lang N. D , Fred L.D .Nano Letters, 8 (2008) 2446

22 Ni ZH, Wan C.C , Carlo A.D .Nano Letters , 7 (2007) 2763

23 Geim AK, Novoselov KS. Nature Mater, 6 (2007) 686

24 Charlier JC, Blase X, and Roche S. Rev. Mod. Phys. 79 (2007) 732

25 Han MY. Phys. Rev. Lett., 98 (2007) 206805

26 Li X, Wang X, Zhang L, Lee S, Dai H. Science, 319 (2008) 1232

27 Han MY, Ozylmaz B, Zhang Y, Kim P. Phys. Rev. Lett. 98 (2007) 206805

28 Ouyang FP, Huang B, Li ZY, Xiao J, and Xu H. J. Phys. Chem. C, 112 (2008) 12007

29 Schedin F, Geim AK, Morozov SV, Hill EW, Blake P, Katsnelson MI, Novoselov K. Nat. Mater.5 (2007) 652

30 Williams JR, DiCarlo LC, and Marcus CM. Science 317 (2007) 641

31 Katsnelson MI, Novoselov KS, and Geim AK. Nat. Phys. 2 (2006) 625

32 Cheianov VV, Falko VI, Altshuler BL. Science, 315 (2007) 1255

33 Dutta S, Lakshmi S, and Pati SK. Phys. Rev. B:77 (2008) 073412

34 Wang ZF, Li Q, Zheng H, Ren H, Su H, Shi QW, and Chen J. Phys. Rev. B:75 (2007) 113406

35 Son YW, Cohen ML, and Louie SG. Phys. Rev. Lett, 97 (2006) 216803

36 Shemella P, Zhang Y, Mailman M, Ajayan PM, Nayak SK. Appl. Phys. Lett, 91 (2007) 042101

37 Kunstmann J, Özdogan C, Quandt A, Phys. Rev. B, 83 (2011) 045414

38 Bhandary S, Eriksson O, Sanyal B. Complex edge effects in zigzag graphene nanoribbons due to hydrogen loading. Phys. Rev. B, 82 (2010) 165405

39 Lee G, Cho K. Phys. Rev. B, 79 (2009) 165440

40 Liu Y, Baek JB, Dai LM. ACS Nano, 4 (2010) 1326

41 Li XL, Wang HL, Robinson JT, Sanchez H, Diankov G, Dai HJ. J. Am.Chem. Soc. 131 (2009) 15944

42 Gong KP, Du F, Xia ZH, Durstock M, and Dai LM. Science, 323 (2009) 764

43 Shao YY, Sui JH, Yin GP, and Gao YZ. Appl. Catal. B,79 (2008) 99

44 Deng SY, Jian GQ, Lei JP, Hu J, and Ju HX. Biosens. Bioelectron. 25 (2009) 377

45 Ozaki T, Nishio K, Wang H, et al. Phys. Rev. B, 81 (2010) 074522

46 Cong C, Yu T, and Wang H. ACS Nano, 4 (2010) 3175

47 Wang X, Li X, Zhang L, Yoon Y, Weber PK, Wang H, Guo J, Dai H. Science,7 (2009) 768

48 Giovannetti G, Khomyakov PA, Brocks G, Karpan VM, Van den Brink J. Phys. Rev. B, 60 (1999) 5608

49 Zeghbroeck BV. Principles of Semiconductor Devices, Colarado University, Colarado, 5 (2011) 69

50 Chang QS, Tay BK, Li S, Sun XW, Lau SP, Chen TP. Mater. Phys. Mech, 4 (2001) 134

51 Babic B and Schonenberger C. Phys. Rev.B: 70 (2004) 19540

52 Fano U. Phys. Rev. 12 (1961) 41866

53 Shi X, Dai Z, Zeng Z. Phys. Rev. B, 76 (2007) 235412

54 Miroshnichenko AE, Flach S,Kivshar YS, Rev of Mod. Phys,8 (2010) 2257

55 Nitzan A, Ratner M.A. Science, 300 (2003) 1384

56 Dai ZX, Shi XQ, Zheng XH, Wang XL and Zeng Z. Phys. Rev. B, 75 (2007) 155402

57 Lee YJ, Brandbyge M, Puska MJ, Taylor J, Stokbro K, Nieminen RM. Phys Rev, B: 69 (2004) 125409

58 Liang W, Chapman C.T, Frisch M.J, Li X, Chem J. Theory Comput, 6 (2010) 3352

59 Hartree DR, Proc. Cambridge Phil. Soc., 24 (1928)426

60 Zyilmaz B, Jarillo HP, Efetov D, Abanin DA, Levitov LS, Kim P. Phys. Rev. Lett. 6 (2007) 99

61 Thomas LH. Proc. Cambridge Phil. Roy. Soc., 23 (1927) 542

62 Hohenberg P. and Kohn W, Phys. Rev. 136 (1964) 871

63 Kohn W and Sham LJ . Phys.Rev.140 (1965) 1133

64 Brandbyge M, Mozos J, Ordejon P, Taylor J, Stokbro K. Phys.Rev., 65 (2002) 165401

65 Boukhvalov DW, Katsnelson MI. Nano Lett. 8 (2008) 4379

66 Buttiker M, Imry Y, Landauer.Phys. Rev. B, 31 (1985) 6215

67 ATK Tutorial and Reference Guide, Version 2.0 (2006) URL:http://www.quantumwise.com,/manualsandTutorial/ATK2.0.4.Retrieved on June, 20, 2011

68 ATK Tutorial for Device Configurations, Version 11.2.2 (2011) URL:http://www.quantumwise.com/manuals/atk11.2.2TutorialandReference Retrieved on June, 12, 2011

69 VNL: Tutorial, Version 11.2.2 (2011)

URL:http://www.quantumwise.com/manuals/atk11.2.2TutorialandReference

Retrieved on June, 12, 2011

70 Jian DL, Bin C, Jie Z, Li JZ, Hui MW, Bang JY .Chin.Phys.20 (2011) 108105.

71 VNL: Tutorial, Version 2008.10 (2008)

URL: http://www.quantumwise.com/documents/manuals/vnl-(2008)10tutorial,

Retrieved on June, 20, 2011

72 Kan E J, Li X, Yang J, Hou JG. Appl. Phys. Lett. 91 (2007) 243116

73 Yan HZ,Xiao HZ,Zhao YZ , J. Phys.Cond. Matt, 20 (2008) 045225

74 Brian L, Jeremy T, Mehrez H, Hong G. Phys. Rev. B, 64 (2001) 075420